nature communications

Article

https://doi.org/10.1038/s41467-025-64860-7

Wild-type KRAS activation drives evasion of interferon-mediated immunity and resistance to immunotherapy in hepatocellular carcinoma

Received: 26 October 2024

Accepted: 30 September 2025

Published online: 11 November 2025

Check for updates

Martina Mang Leng Lei[1], Carmen Oi Ning Leung[1], Rainbow Wing Hei Leung[1], Xue Qian Wu[1], Katherine Po Sin Chung[1], Catherine Yu Jia Gu[1], Mandy Sze Man Chan[1], Wing Ki Chau[1], Quan Hua Mu[1], Kai Yu Ng[2], Man Tong[3], Jing Ping Yun[4], Jia Ming Nickolas Teo[2], Guang Sheng Ling[2,5], Patrick Pak Chun Wong[3], Stephen Lam Chan[6], Zhe Wen Xiong[3], Alfred Sze Lok Cheng[3], Jin Ding[7], Stephanie Ma[2,8] & Terence Kin Wah Lee[1,9]

Increasing evidence indicates that activation of oncogenic pathways contributes to an unfavourable tumour immune microenvironment (TIME), ultimately resulting in resistance to immunotherapy. Here, we aim to identify a critical oncogenic pathway involved in an antigen-expressing *c-MYC-lucOS*^{OE}/*Tp53*^{KO} hepatocellular carcinoma (HCC) mouse model that simulates immune response against tumour-associated antigens. Using data-independent acquisition proteomics, we reveal the role of wild-type KRAS in immune escaped mouse HCC tumours, with EGF concurrently activating EGFR/MEK/ERK signalling. Single cell RNA sequencing data analysis reveals that KRAS signalling intrinsically inhibits interferon-mediated MHC-I expression and extrinsically impairs CD8$^+$ T cell activity due to the suppression of CXCL9 through the EGFR/MEK/ERK pathway. We observe KRAS activation in HCC patients who received immune checkpoint inhibitor (ICI) treatments, where it correlates with poor clinical outcomes. Notably, combination therapy with SOS1 inhibitor MRTX0902, Trametinib, and anti-PD-1 antibody effectively increased intratumoural CD8$^+$ T cell infiltration and improved survival. Our study thus reveals that targeting wild-type KRAS signalling in combination with ICIs may serve as an effective treatment strategy for advanced HCC patients.

Hepatocellular carcinoma (HCC) is the third most lethal cancer and the sixth most commonly diagnosed cancer worldwide[1]. Improved survival rates have been achieved through recent advancements in HCC systemic therapy, particularly with the emergence of immune checkpoint inhibitors (ICIs)[2–6]. The IMBrave-150 trial demonstrated the superior efficacy of combining anti-PD-1 and anti-vascular endothelial growth factor (VEGF) monoclonal antibodies (atezolizumab and bevacizumab) for treating advanced HCC. This combination resulted in a notably high objective response rate (~27%) and an improvement in overall survival compared to sorafenib (19.2 months vs. 13.4 months)[4]. The success of targeting the PD-L1/PD-1 pathway in

A full list of affiliations appears at the end of the paper. e-mail: terence.kw.lee@polyu.edu.hk

HCC has led to the exploration of new treatments that incorporate ICIs as standard therapies for HCC patients.

However, anti-PD-1 monotherapies benefit only a subset of patients, with overall response rates of 20% or less[7]. Among tumour-intrinsic properties such as mutation load and tumour antigen expression, the immune evasive mechanisms of oncogenic pathways are gaining increasing attention. This is due to the growing understanding that these mechanisms can lead to resistance to anti-PD-1 therapy. For instance, activation of β-catenin (encoded by *CTNNB1*)[8] or deletion of *PTEN*[9] in melanoma and prostate cancer can cause T cell exclusion and resistance to anti-PD-1 therapy. In HCC, β-catenin activation is associated with T-cell exhaustion[10,11] and evasion[12]. Recently, the activation of tumour-intrinsic cell cycle-related kinase (CCRK)[13], hypoxia-inducible factor 1-alpha (HIF-1α)[14] and oncogenic *c-MYC*[15] has been shown to facilitate immune evasion in HCC by recruiting immunosuppressive cells, such as myeloid-derived suppressor cells (MDSCs) and proinflammatory macrophages. Therefore, identifying the intrinsic oncogenic signalling pathways that drive immune evasion can enhance the efficacy of anti-PD-1 therapy in HCC.

Herein, we show wild-type KRAS signalling as one of the key pathways upregulated in immune-escaped *c-MYC-lucOS^{OE}/Tp53^{KO}* HCC mouse model. Using data-independent acquisition mass spectrometry (DIA-MS), we demonstrate that wild-type KRAS overexpression, accompanied by EGF-mediated activation of the EGFR/MEK/ERK axis, drives immune evasion in this model. Mechanistically, KRAS suppresses both intrinsic and extrinsic interferon (IFN) responses, dampening DC and CD8 T cell recruitment. Using a KRAS-driven immune-escaped HCC tumour model, in vivo MEK1/2 knockout and pharmacological inhibition with SOS1 inhibitor MRTX0902 and Trametinib, promote intratumoral CD8$^+$ T-cell infiltration and sensitise the tumour to anti-PD-1 therapy, improving survival outcomes. These findings offer new perspectives on targeting wild-type KRAS to overcome resistance to immune checkpoint blockade.

Results

Expression of exogenous antigens delays tumour progression in the *c-MYC-lucOS^{OE}/Tp53* HCC mouse model

Given the high co-alteration frequency of oncogene *MYC* and tumour suppressor *TP53* (21%; 69/338 in the TCGA-HCC) and (27%; 60/239 in the CLCA cohort) in HCC (Supplementary Fig. 1a)[16,17], we established an immunocompetent *c-MYC-luc^{OE}/Tp53^{KO}* murine HCC model to represent a significant portion of HCC cases with these molecular signatures. To understand the immune evasive mechanism in HCC, T-cell epitope antigens SIYRYYGL (SIY), SIINFEKL (SIN, OVA257-264), and OVA323-339 were incorporated into the C-terminus of the oncogenic *c-MYC*-expressing plasmid (*c-MYC-lucOS^{OE}*), mimicking tumour-associated antigens (TAAs). These exogenous antigens have been reported to induce an anti-tumour CD8$^+$ T cell immune response in the *c-MYC-luc^{OE}/Tp53^{KO}* HCC model[12]. The pT3-EF1A-c-MYC-luc construct (with or without antigens) was introduced into the hepatocytes of C57BL/6 mice via hydrodynamic tail veil injection (HTVI) with SB13 transposase, alongside a CRISPR-Cas9 vector targeting *Tp53* (Supplementary Fig. 1b). Control mice *c-MYC-luc^{OE}/Tp53^{KO}* showed progressive tumour growth, with increasing bioluminescence signals from day 3 to day 31 (Fig. 1a, b). All the *c-MYC-luc^{OE}/Tp53^{KO}* mice presented gross liver tumours, with a median survival of 42 to 48 days (Fig. 1c). In contrast, the luciferase signals of the antigen-expressing *c-MYC-lucOS^{OE}/Tp53^{KO}* group declined significantly on day 31 (Fig. 1a, b). 80% (8/10) of mice did not develop any tumours within 60 days (Fig. 1c, d). However, the anti-tumour T-cell response failed to clear tumour cells in all mice, and 20% (2/10) of mice developed tumours, suggesting partial evasion of T-cell surveillance.

DIA proteomic analysis reveals oncogenic KRAS signalling enriched in the *c-MYC-lucOS^{OE}/Tp53^{KO}* HCC mouse model of immune evasion

To identify the intrinsic oncogenic pathway associated with immune evasion, tumour tissues were harvested from *c-MYC-luc^{OE}/Tp53^{KO}* mice and immune-escaped *c-MYC-lucOS^{OE}/Tp53^{KO}* mice ($n = 5$/group) for DIA proteomics (Supplementary Fig. 1c, d). Gene Set Enrichment Analysis (GSEA) was performed to assess the oncogenic pathways enriched in immune-escaped tumours. First, GOBP_ADAPTIVE_IMMUNE_RESPONSE was enriched in immune-evaded tumour, confirming antigen-induced immune activation (Supplementary Fig. 1e). In the H: Hallmark gene sets database (Fig. 1e and Supplementary Table 1), ten gene sets were significantly ($p < 0.05$) enriched in *c-MYC-lucOS^{OE}/Tp53^{KO}* group, including immune-related hallmarks: Complement, IL2/STAT5 and TNF/NF-κB signalling. Aligned with previous report[12] showing an enrichment of Wnt pathway-related gene set in *c-MYC-lucOS^{OE}/Tp53^{KO}* tumours (Supplementary Fig. 1f), we intriguingly found that oncogenic KRAS signalling (KRAS_SIGNALLING_UP) was the top oncogenic pathway among the enriched pathways (NES = 2.01, $p = 0.0002$; Fig. 1f). Moreover, the protein levels of KRAS (log2FC = 1.44) and its downstream effector cyclin D1 (CCND1; log2FC = 2.915) were increased in *c-MYC-lucOS^{OE}/Tp53^{KO}* tumours (Fig. 1g). RT-qPCR analysis also confirmed the upregulation of *Kras* mRNA expression in immune-escaped tumours (Supplementary Fig. 1g). Immunohistochemical (IHC) analysis demonstrated higher expressions of upstream pEGFR, KRAS and pERK1/2 in *c-MYC-lucOS^{OE}/Tp53^{KO}* tumours, with colocalization of KRAS with pERK1/2 (Fig. 1h) and HNF4a (Supplementary Fig. 1h), confirming the activation of EGFR/KRAS/ERK signalling in *c-MYC-lucOS^{OE}/Tp53^{KO}* HCC tumour cells.

Wild-type KRAS expression is upregulated in HCC samples and is correlated with a poor prognosis

Unlike other cancer types, *KRAS* mutations are rare in liver cancer[17]. The frequency of *KRAS* mutation occurs in only approximately 1.18-17.82% of HCC cases (Supplementary Table 2). In the TCGA-HCC cohort, wild-type *KRAS* mRNA expression was upregulated in 355 primary HCC tumours compared to 49 normal liver tissue samples (mean log2(TPM + 1): 3.164 vs 2.818, $p < 0.0001$), with stepwise upregulation observed as cancer stage increased (Supplementary Fig. 2a, b). HCC patients with high *KRAS* expression have poorer overall survival outcomes (HR = 1.638, 95% CI = 0.969-2.767, $p = 0.0653$; Supplementary Fig. 2c). IHC analysis of a tissue microarray with 51 clinical HCC samples was performed to compare KRAS protein level (Supplementary Fig. 2d). Patients with KRAS overexpression (26/51 cases) had a higher likelihood of experiencing HCC relapse (76% in high KRAS vs 16% low KRAS; Supplementary Fig. 2e) and a poorer disease-free survival rate (HR = 4.704, 95% CI = 2.005 to 11.04, $p = 0.0004$; Supplementary Fig. 2f).

Wild-type KRAS overexpression abolishes the anti-tumour T-cell response and promotes immune evasion in the *c-MYC-lucOS^{OE}/Tp53^{KO}* model

To validate the hypothesis that KRAS signalling promotes immune evasion, we overexpressed wild-type *Kras* in the *c-MYC-lucOS^{OE}/Tp53^{KO}* HCC. Notably, all (100%) of *c-MYC-lucOS^{OE}/Tp53^{KO}/Kras* mice developed tumours which exhibit HCC phenotype in both morphology and molecular characteristics, demonstrating complete escape from immune surveillance (Fig. 2a–e and Supplementary Fig. 3). KRAS-mediated immune evasion occurs through EGFR/ERK pathway activation, as evidenced by increased phosphorylation of both EGFR and ERK1/2 in antigen-expressing *c-MYC-lucOS^{OE}/Tp53^{KO}* tumours (Fig. 2f, g and Supplementary Fig. 4). To activate wild-type KRAS signalling, we believe that this process is mediated by receptor tyrosine kinase (RTK) ligands, such as EGF, TGF-α, and HGF. We observed that EGF was most significantly upregulated in antigen-expressing *c-MYC-lucOS^{OE}/Tp53^{KO}* models (Fig. 2h and Supplementary Fig. 5a, b), which is consistent with

https://doi.org/10.1038/s41467-025-64860-7

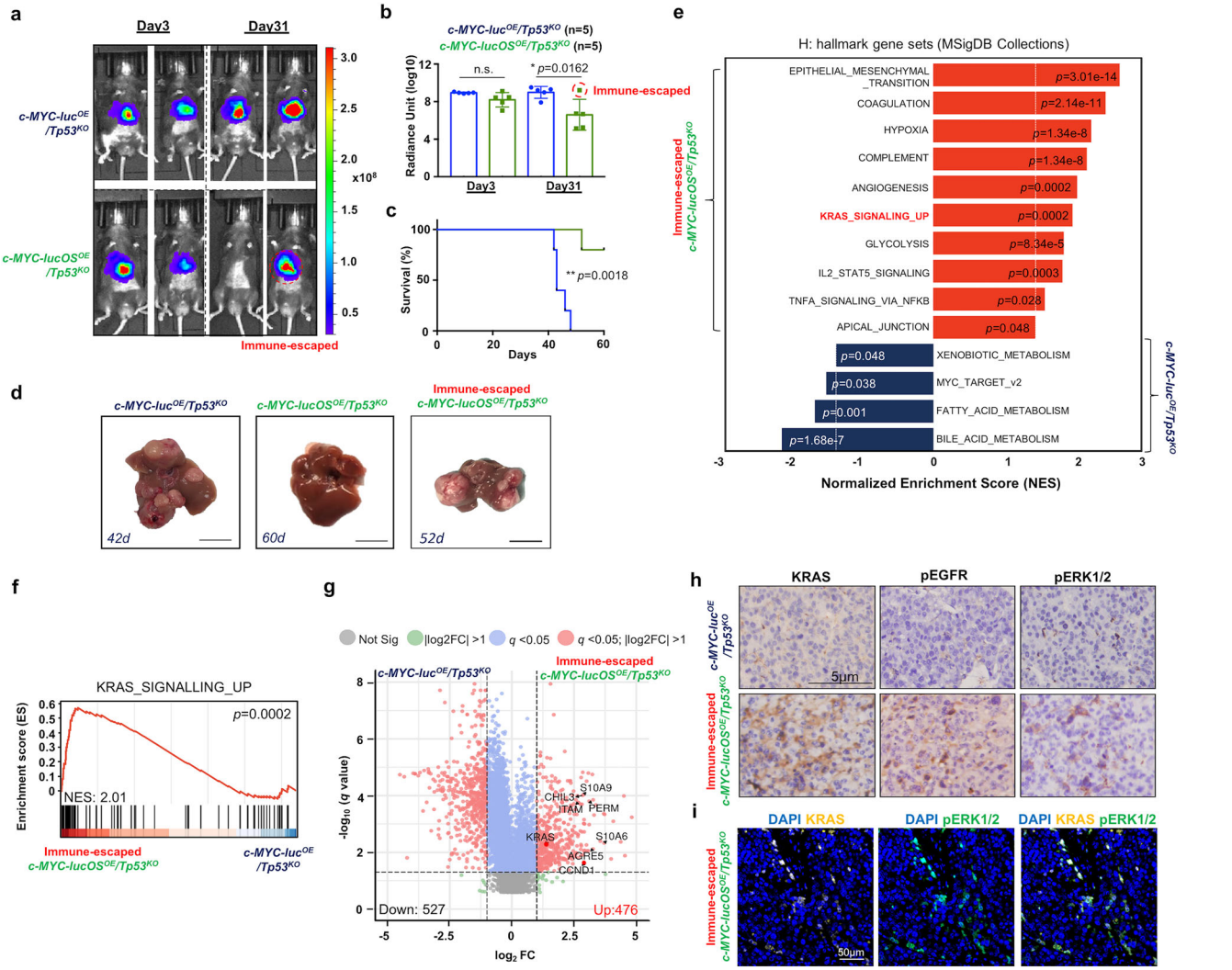

Fig. 1 | DIA proteomic analysis reveals KRAS pathway activation enriched in the *c-MYC-lucOS^{OE}/Tp53^{KO}* HCC mouse model of immune escape. a Representative bioluminescence images and **b** quantification of normalised luciferase signals of *c-MYC-luc^{OE}/Tp53^{KO}* and *c-MYC-lucOS^{OE}/Tp53^{KO}* mice at day 3 and day 31 post-HTVI (two-sided unpaired *t* test). **c** Survival analysis (log-rank Mantel–Cox test). **d** Liver images of *c-MYC-luc^{OE}/Tp53^{KO}* and *c-MYC-lucOS^{OE}/Tp53^{KO}* and immune escaped *c-MYC-lucOS^{OE}/Tp53^{KO}* mice. Scale bar = 1 cm. $n = 5$ mice/ group examined over 2 independent experiments. **e** Gene Set Enrichment Analysis (GSEA) of significantly dysregulated pathways (H: hallmark gene sets database from MSigDB Collections, $p < 0.05$) in immune-escaped *c-MYC-lucOS^{OE}/Tp53^{KO}* tumours versus *c-MYC-luc^{OE}/Tp53^{KO}* tumours (one-sided Kolmogorov–Smirnov test). NES = Normalised Enrichment Score. **f** Enrichment of KRAS_SIGNALING_UP in immune-escaped *c-MYC-lucOS^{OE}/Tp53^{KO}* tumours (one-sided Kolmogorov–Smirnov test). **g** Volcano plot of differentially expressed proteins (log2 FC vs −log10 *q*-value) in tissues of immune-escaped *c-MYC-lucOS^{OE}/Tp53^{KO}* tumours versus *c-MYC-luc^{OE}/Tp53^{KO}* tumours. Dashed lines: thresholds ($q < 0.05$, $|\log_2 FC| > 1$). Red points highlight KRAS (log2FC: 1.44, $q = 0.005$) and CCND1 (log2FC: 2.915, $q = 0.025$) upregulated in immune-escaped *c-MYC-lucOS^{OE}/Tp53^{KO}* tumours (two-sided unpaired *t* test with adjusted *q*-value). $n = 5$ biologically independent samples/ group. FC = Fold Change. **h** IHC staining reveals upregulated pEGFR, KRAS and pERK1/2 in immune-escaped *c-MYC-lucOS^{OE}/Tp53^{KO}* tumour tissues compared to controls, indicating pathway activation. **i** Multiplex IHC colocalization of KRAS (yellow) and pERK1/2 (green) confirms KRAS activation in immune escape. $n = 2$ independent experiments. Scale bar = 5 μm, 50 μm. Data are presented as mean ± SD. * $p < 0.05$, ** $p < 0.01$, n.s. = not significant. Source data are provided as a Source Data file.

the increased levels of pEGFR and pERK1/2. This finding is further supported by the enrichment of the BORLAK_LIVER_CANCER_EGF_UP signature (NES = 2.19, $p = 0.00002$) in *c-MYC-lucOS^{OE}/Tp53^{KO}* model (Supplementary Fig. 5c). Multiplex IHC analysis localised EGF production is derived from tumour-infiltrating CD11c^{+} dendritic cells (Supplementary Fig. 5d, e). Together, these results indicate that upon stimulation with EGF, wild-type KRAS overexpression promotes immune evasion via the activation of the EGFR/KRAS/ERK axis.

scRNA-seq revealed that KRAS shapes an immunosuppressive tumour immune microenvironment (TIME) via dampening IFN responses and antigen presentation

The TIME of the *c-MYC-lucOS^{OE}/Tp53^{KO}/EV* and *c-MYC-lucOS^{OE}/Tp53^{KO}/Kras* mice were compared using scRNA-seq (Fig. 3a, b and Supplementary Fig. 6a). Immunophenotypic analysis of wild-type KRAS overexpressing tumours reveals a profound remodelling of the TIME, characterised by predominant immunosuppressive myeloid cells populations and a remarkable reduction in anti-tumorigenic T cells as well as NK cells (Fig. 3c). Wild-type KRAS exerts an immunosuppressive effect on the TIME, including downregulation of IFN responses and lymphocyte chemotaxis, and antigen processing and presentation (Fig. 3d). Priming of lymphocytes by professional antigen-presenting cells (APCs) is essential for initiating adaptive immune responses. Pathway analysis of the DC population revealed KRAS-dependent suppression of IFN-α (NES: 1.74, $p = 0.01$) and IFN-γ (NES: 1.58, $p = 0.01$) responses (Fig. 3e). This impairment in IFN signalling consequently led to a significant reduction in the 'Antigen processing and presentation machinery' signature (NES: 1.99,

https://doi.org/10.1038/s41467-025-64860-7

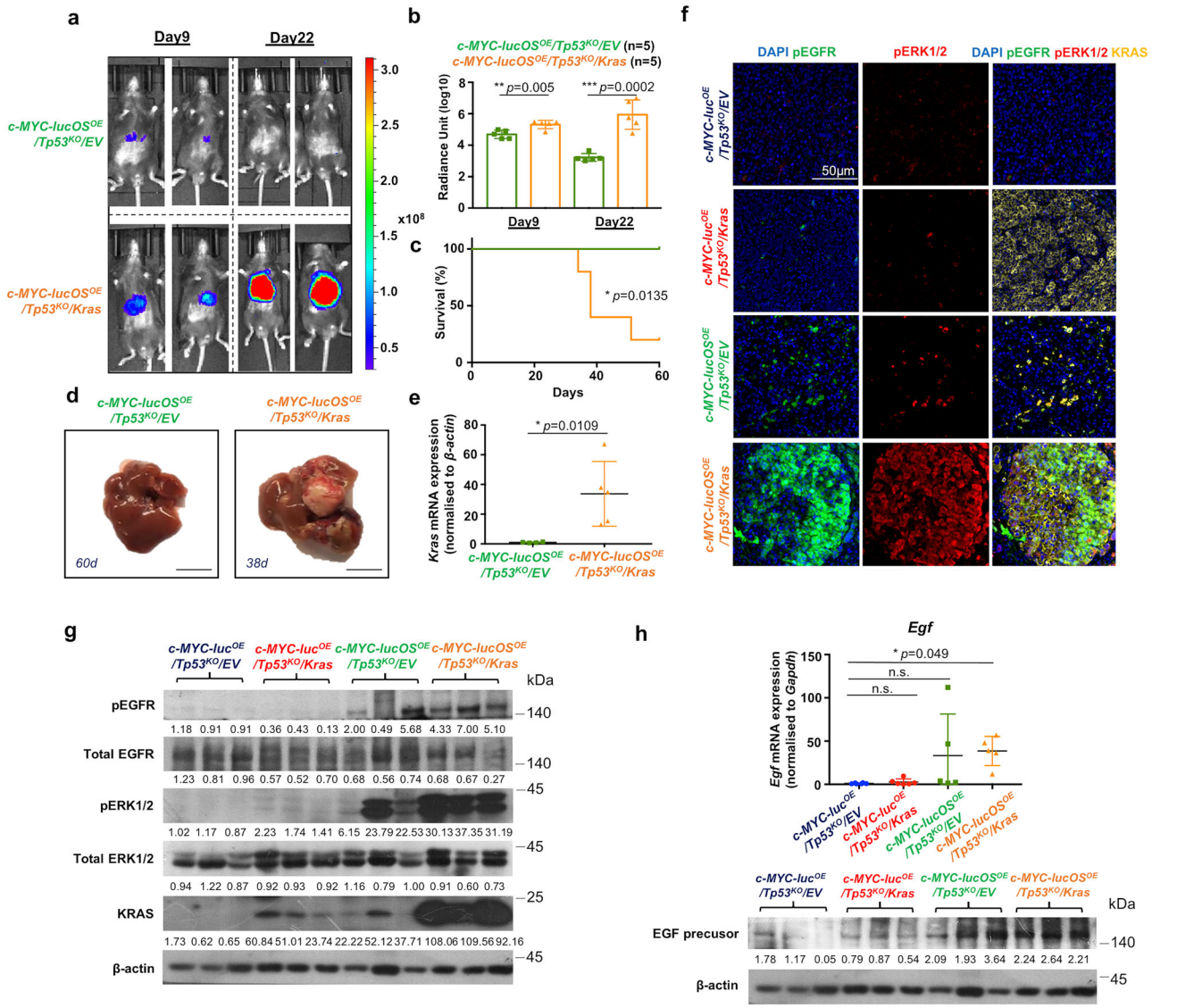

Fig. 2 | Wild-type *Kras* overexpression drives immune evasion via EGF/EGFR/KRAS/ERK signalling activation. a Representative bioluminescence images and **b** quantification of normalised luciferase signals of *c-MYC-lucOS^{OE}/Tp53^{KO}/EV* and *c-MYC-lucOS^{OE}/Tp53^{KO}/Kras* mice at day 9 and day 22 post-HTVI (two-sided unpaired *t* test). **c** Survival analysis (log-rank Mantel–Cox test). **d** Liver images of *c-MYC-lucOS^{OE}/Tp53^{KO}/EV* and *c-MYC-lucOS^{OE}/Tp53^{KO}/Kras* mice. Scale bar = 1 cm. $n = 5$ mice/group examined over 2 independent experiments. **e** RT-qPCR validation of wild-type *Kras* mRNA overexpression in *c-MYC-lucOS^{OE}/Tp53^{KO}/Kras* tumours (two-sided unpaired *t* test). $n = 5$ biologically independent samples/ group. **f** Multiplex IHC and **g** western blot demonstrating activation of EGFR/KRAS/ERK signalling in immune escaped *c-MYC-lucOS^{OE}/Tp53^{KO}/EV* and *c-MYC-lucOS^{OE}/Tp53^{KO}/Kras* tumours ($n = 3$). Scale bar = 50 μm. **h** RT-qPCR and western blot showing EGF upregulation in *c-MYC-lucOS^{OE}/Tp53^{KO}/EV* and *c-MYC-lucOS^{OE}/Tp53^{KO}/Kras* tissues (one-way ANOVA). *c-MYC-luc^{OE}/Tp53^{KO}/EV* and *c-MYC-luc^{OE}/Tp53^{KO}/Kras*: $n = 6$ biologically independent samples/ group; *c-MYC-lucOS^{OE}/Tp53^{KO}/EV* and *c-MYC-lucOS^{OE}/Tp53^{KO}/Kras* group: $n = 5$ biologically independent samples/ group. Data are presented as mean ± SD. * $p < 0.05$, ** $p < 0.01$, *** $p < 0.001$, n.s. = not significant. Source data are provided as a Source Data file.

$p = 0.001$)[18]. Furthermore, key components of the IFN-induced antigen-presenting machinery (APM), including *Nlrc5*, *B2m*, *Tap1*, *Cd74*, and *Ciita*, were downregulated in KRAS-overexpressing tumours (Fig. 3f and Supplementary Fig. 6b). Beyond defective T cell recruitment, KRAS overexpression also diminished the proportion of IFN-stimulated (CD8-c5-Ifit3) and proliferative (CD8-c4-Mki67) CD8$^+$ T cells among the CD8 T cell population (Fig. 3g, h and Supplementary Fig. 6c, d). The loss of IFN-stimulated CD8$^+$ T cells (*Ifit3$^+$Ifit1$^+$Isg15$^+$*), which typically exhibit enhanced cytotoxic activity and increased MHC-I expression, compromises direct tumour cell killing. Furthermore, reduced proliferative capacity (*Mki67$^+$Stmn1$^+$Ube2c$^+$*) in CD8$^+$ T cells indicates impaired clonal expansion, which is essential for amplifying anti-tumour response. Together, these mechanisms establish a permissive tumour microenvironment that subverts anti-tumour immunity and promotes immune evasion. Notably, these findings align with impaired IFN-α (NES:1.89, $p < 0.0001$) and IFN-γ (NES:1.45, $p = 0.0143$) responses observed in KRAS-high HCC patients in the TCGA-HCC cohort (Supplementary Fig. 6e), alongside a negative correlation with the infiltration of CD8$^+$ T cells (Supplementary Fig. 6f), suggesting that the KRAS-mediated immunosuppressive mechanism is clinically relevant.

Wild-type KRAS activation promotes immune evasion via suppression of DC and T cell recruitment to the tumour site

To investigate how wild-type KRAS modulates adaptive immunity, we tracked changes in bioluminescence signals and SIINFEKL-specific CD8$^+$ T cells in *c-MYC-lucOS^{OE}/Tp53^{KO}/EV* and *c-MYC-lucOS^{OE}/Tp53^{KO}/Kras* mice during the first two weeks after HTVI (Fig. 4a). In the second week, the bioluminescence signals in the *c-MYC-lucOS^{OE}/Tp53^{KO}/EV* group began to decrease, indicating the initiation of an

https://doi.org/10.1038/s41467-025-64860-7

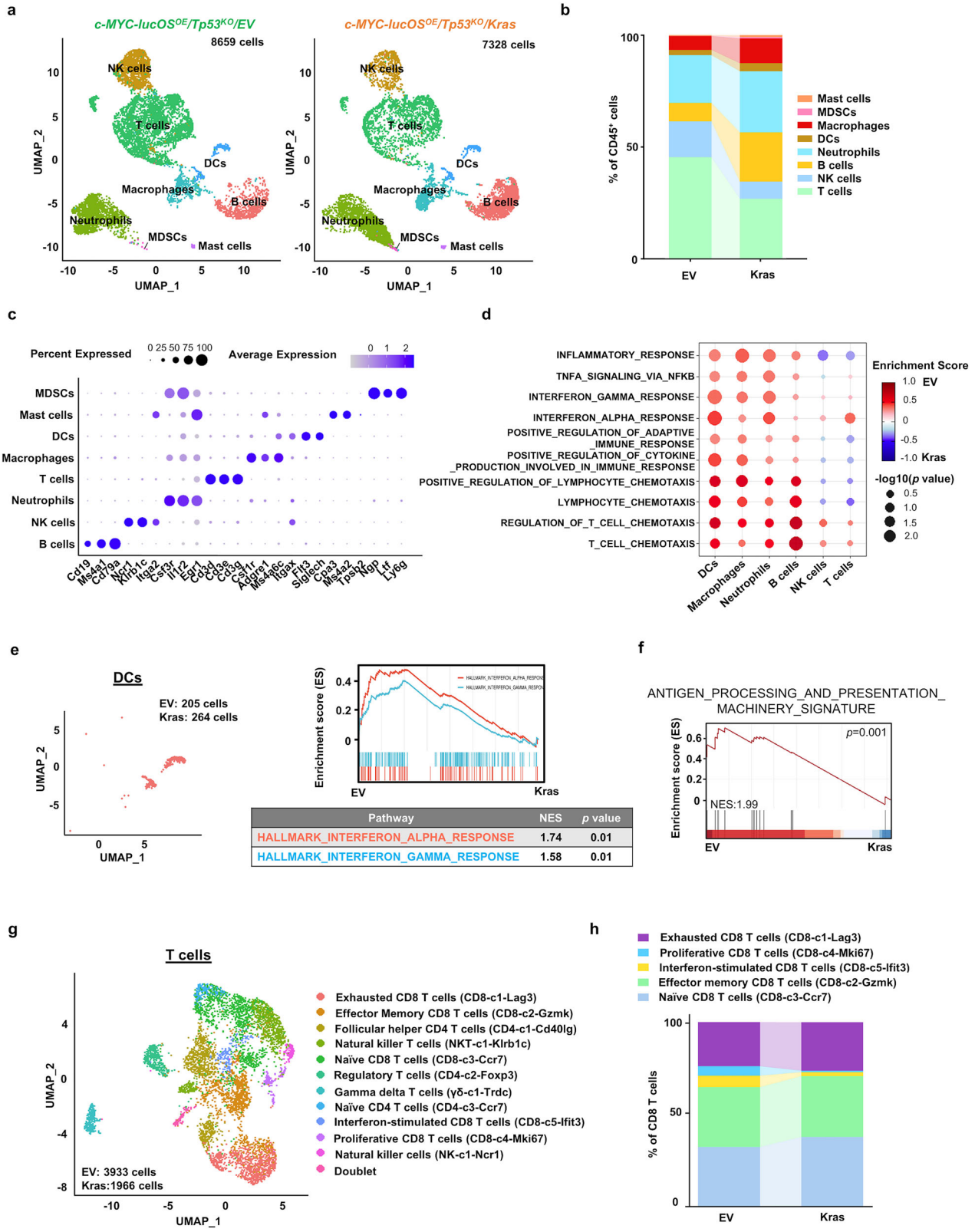

anti-tumour immune response. The antigen-specific response was further supported by the detection of SIINFEKL-specific CD8$^+$ T cells (CD45$^+$TCR-b$^+$CD8$^+$H-2Kb-SIINFEKL$^+$), thus, we performed immune profiling (Supplementary Fig. 7a, Supplementary Table 3). Consistent with scRNA-seq findings, KRAS-overexpressing livers exhibit profound defects in adaptive immunity, characterised by predominant immunosuppressive myeloid cells, impaired T cell recruitment and DC dysfunction (Fig. 4b). Intriguingly, we observed a reduction in DC numbers, with SIINFEKL-specific CD8$^+$ T cells diminished to about one-third that in the EV group (Fig. 4c). In addition, CD4$^+$ (CD45$^+$TCR-b$^+$CD4$^+$) and CD8$^+$ (CD45$^+$TCR-b$^+$CD8$^+$) T cells exhibited lower (CD44$^+$) activation (Supplementary Fig. 7b). To confirm that wild-type KRAS drives immune evasion in a GTP-binding-dependent manner, we introduced a KRAS mutant KRASS17N that cannot bind

Fig. 3 | KRAS-mediated suppression of interferon responses impairs immune activation and antigen presentation in the tumour immune microenvironment (TIME). a Uniform manifold approximation and projection (UMAP) showing CD45$^+$ sorted immune cells from the scRNA-seq of *c-MYC-lucOS^{OE}/Tp53^{KO}/EV* and *c-MYC-lucOS^{OE}/Tp53^{KO}/Kras* (EV: 8659 cells, Kras: 7328 cells pooled from $n = 3$ mice/ group). **b** Composition of immune cell clusters showing altered population distributions. **c** Bubble plot of lineage-defining genes for major immune cell subtypes. **d** Bubble plot showing KRAS exerts an immunosuppressive effect on the TIME, including downregulation of inflammatory response, interferon signalling and T cell chemotaxis (one-sided Kolmogorov–Smirnov test). **e**, **f** DC subcluster analysis (EV: 205 cells; Kras: 264 cells) demonstrating reduced interferon responses and antigen processing and presentation machinery in the Kras group as compared to EV control (one-sided Kolmogorov–Smirnov test). **g** T cell subclusters (EV: 3933 cells; Kras: 1966 cells) showing reduced infiltration in the Kras group. **h** Altered proportions of exhausted (CD8-c1-Lag3), effector memory (CD8-c2-Gzmk), naïve (CD8-c3-Ccr7), proliferative (CD8-c4-Mki67) and interferon-stimulated (CD8-c5-Ifit3) CD8 T cell populations between EV versus Kras tumours. Source data are provided as a Source Data file.

GTP. The expression of KRAS S17N in the *c-MYC-lucOS^{OE}/Tp53^{KO}* model failed to drive immune evasion and restored the infiltration of DCs, CD8$^+$ T cells and SIINFEKL-specific CD8$^+$ T cells, confirming that the KRAS-mediated immune exploitation is dependent on GTP binding (Supplementary Fig. 8). To explain the KRAS-mediated immune composition change, we measured the expression of cytokines and chemokines. The expression of *Ccl3* was significantly higher in the *c-MYC-lucOS^{OE}/Tp53^{KO}/Kras* group (Fig. 4d), echoed the enhanced recruitment of myeloid cells, including monocytes, macrophages and neutrophils (Supplementary Fig. 7b). Interestingly, the levels of IFN-inducible inflammatory chemokines, *Ccl5*, *Cxcl9*, and *Cxcl11*, were significantly decreased in the *Kras* group[19]. CCL5 is responsible for the DC recruitment, whereas CXCL9 and CXCL11 act as T cell chemoattractants at the tumour site[20,21]. This chemokine dysregulation coincided with downregulation of IFN signalling components (*Stat1*, *Stat2*, *Irf1*, *Irf2* and *Irf9*) in the *c-MYC-lucOS^{OE}/Tp53^{KO}/Kras* tumours, supporting our model wherein wild-type KRAS activation suppresses extrinsic IFN responses to impair DC and T cell trafficking to the TIME. ScRNA-seq analysis of HCC patients ($n = 71$) independently confirmed the phenotype of reduced infiltration of antigen-presenting DC subsets (DC_01_CLEC9A and DC_02_CD1C) and attenuated CD8 T cell signature in high KRAS expressors (Supplementary Fig. 9)[22].

Wild-type *Kras* overexpression suppresses MHC-I expression in the *c-MYC-lucOS^{OE}/Tp53^{KO}* HCC mouse model

The negative regulation of oncogenic KRAS/ERK signalling by MHC-I molecules has been widely reported in colorectal, lung and breast cancers[23–25]. Indeed, we observed that the expression of APM genes was inversely correlated with the transcript levels of wild-type KRAS in HCC patients (Fig. 5a). Intriguingly, a negative correlation between KRAS and MHC-I expressions was also found across diverse cancer types (Supplementary Fig. 10a). In our model, we also observed a significant decrease in MHC-I expression in the *c-MYC-lucOS^{OE}/Tp53^{KO}/Kras* tumours compared to that in the EV tumours (Fig. 5b, c). Next, we examined whether similar effects were observed in the cell-based model. Both the mRNA and protein levels of wild-type KRAS are higher in all murine HCC cell lines than in the primary mouse hepatocytes (PMHs; Supplementary Fig. 10b), consistent with earlier observation of elevated wild-type KRAS levels in human HCC tissues (Supplementary Fig. 2a). Hepa-1,6 cells, characterised by high levels of wild-type KRAS and low levels of H-2Kb protein expressions, were treated with IFN-γ (50 ng/ml) and ERK inhibitor U0126 (10 μM) for 24 hours. Treatment of Hepa-1,6 cells with U0126 induced a six-fold increase in H-2Kb expression and further augmented the effect of IFN-γ-induced H-2Kb expression (Fig. 5d). The Hep55.1c cell line, characterised by low KRAS protein level, was chosen as a model for wild-type *Kras* overexpression (Supplementary Fig. 10c). With IFN-γ stimulation (50 ng/ml), wild-type *Kras* overexpression (Kras) had a suppressive effect on H-2Kb surface expression of Hep55.1c cells (Fig. 5e and Supplementary Fig. 10d). Both the EV and Kras groups showed a decrease in H-2Kb expression in a dose-dependent manner with EGF treatment (5 or 10 nM) for both 24 and 48 h (Fig. 5e), indicating that KRAS activation inhibits IFN-induced MHC-I expression in HCC.

In vivo CRISPR/Cas9-mediated MEK1/2 knockout rescues the wild-type KRAS-mediated immunosuppressive TIME and enhances the IFN responses in the *c-MYC-lucOS^{OE}/Tp53^{KO}/Kras* HCC mouse model

To validate whether MEK/ERK signalling mediates KRAS-dependent immune evasion, we used the CRISPR/Cas9 system to deplete MEK1/2 in vivo (Fig. 6a and Supplementary Fig. 11a). The luciferase signals of all groups were comparable on day 5 after HTVI (Fig. 6b, c), yet the signals in the *c-MYC-lucOS^{OE}/Tp53^{KO}/Kras/MEK^{KO}* mice were substantially lower than those in *c-MYC-lucOS^{OE}/Tp53^{KO}/Kras/NTC* mice on day 16, indicating that MEK1/2 knockout effectively alleviated KRAS-mediated tumour progression. The entire group of *c-MYC-lucOS^{OE}/Tp53^{KO}/Kras/NTC* mice escaped immunosurveillance, with a median survival of 21 days. All the mice were harvested on day 30, when all the *c-MYC-lucOS^{OE}/Tp53^{KO}/Kras/NTC* mice died due to high tumour burden. In contrast, only six out of eight mice developed tumours in the *c-MYC-lucOS^{OE}/Tp53^{KO}/Kras/MEK^{KO}* group, which were smaller in size and had fewer nodules (Fig. 6d). Molecular analysis confirmed effective inhibition of KRAS/MEK/ERK signalling and downstream molecules (*Ccnd1* and *Dusp6*) in the *c-MYC-lucOS^{OE}/Tp53^{KO}/Kras/MEK^{KO}* tumours (Fig. 6e, f). Importantly, MEK ablation rescued IFN signalling, restoring the expression of IFN-associated genes such as *Stat1*, *Irf1*, *Irf2*, *Irf7*, and *Irf9*, and T cell chemokines *Cxcl9* and *Cxcl10*. Multiplex IHC revealed increased CD11c$^+$ DC infiltration into the tumour, colocalized with H-2Kb-SIINFEKL expression in MEK^{KO} tumours (Fig. 6g). The observation of CD8$^+$ T cells in close proximity to CXCL9$^+$CD11c$^+$ DCs (Fig. 6h), together with an increase in CD8$^+$ T cell infiltration (Fig. 6i), suggested that MEK blockade promotes CXCL9 production by DCs, thereby facilitating the recruitment of CD8$^+$ T cells within the TIME. Consistent with the increased CD8$^+$ T cell infiltration, cytotoxicity molecules were also significantly upregulated in MEK^{KO} tumours (Supplementary Fig. 11b–d).

Activation of KRAS signalling in anti-PD-1-resistant clinical samples and HCC models

We investigated whether activation of KRAS signalling could reduce the effectiveness of ICIs. We reanalysed the scRNA-seq of the HCC tumour biopsies collected in a phase II clinical trial on pembrolizumab (anti-PD-1; NCT03419481)[26]. Notably, KRAS pathway activity was higher in non-responders than in responders upon anti-PD-1 treatment (Fig. 7a)[27]. In addition, the KRAS pathway was associated with treatment failure and poorer progression-free survival outcomes in patients with HCC treated with atezolizumab (anti-PD-L1; Fig. 7b) in the GO30140 trial[28]. Analysis of our in-house cohort of patients with anti-PD-1-treated HCC further revealed a significantly higher level of EGF in non-responders (Supplementary Fig. 12). Consistent with clinical analyses, we also observed activation of EGFR/KRAS/ERK signalling in non-responsive anti-PD-1-treated *c-MYC-luc^{OE}/Tp53^{KO}* and NAFLD-induced RIL-175 orthotopic HCC mouse models (Supplementary Figs. 13, 14).

https://doi.org/10.1038/s41467-025-64860-7

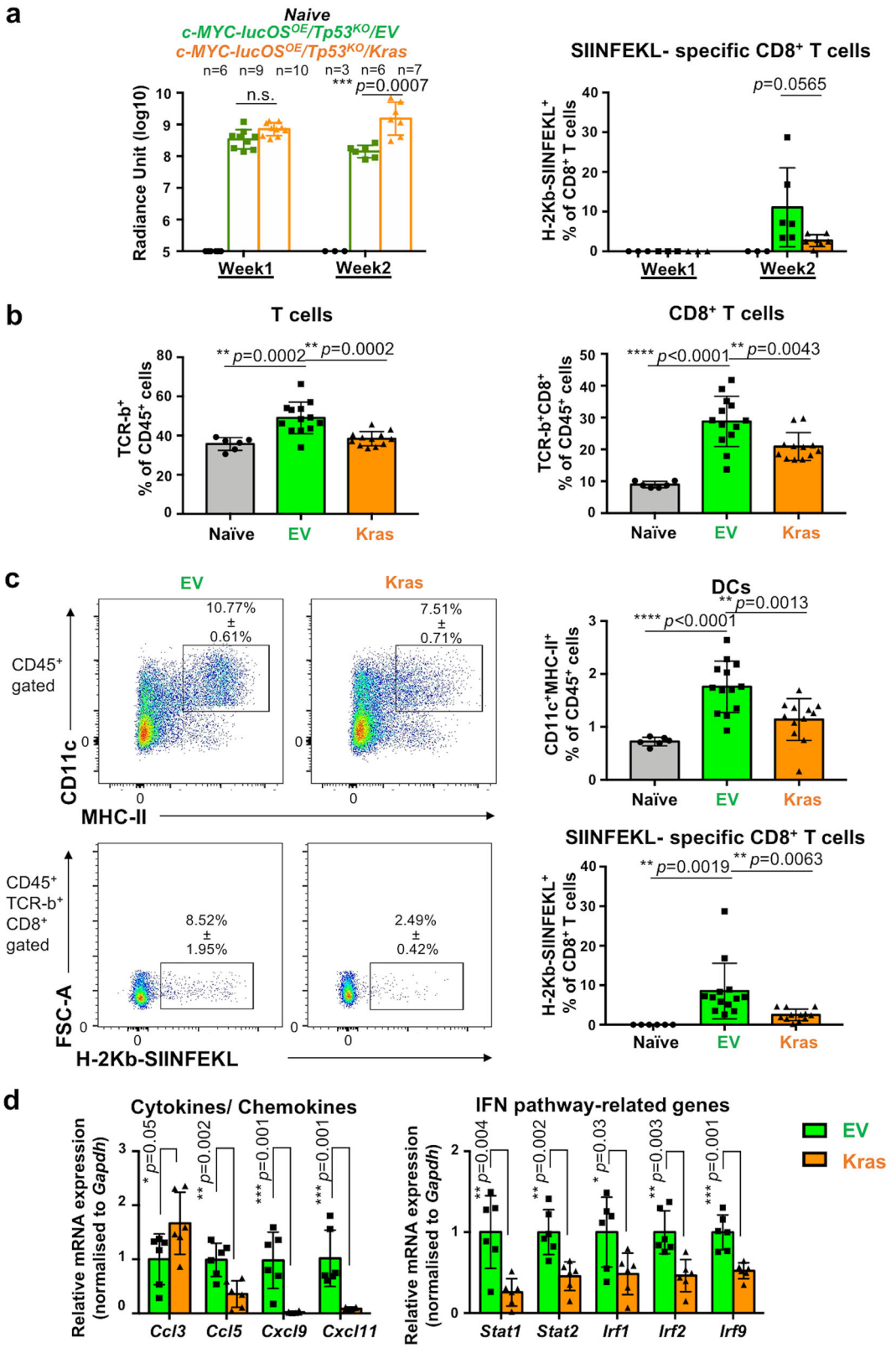

Combination of MRTX0902 and Trametinib with anti-PD-1 suppresses tumour growth and improves survival in the *c-MYC-lucOS^{OE}/Tp53^{KO}/Kras* mouse model

KRAS has been an 'undruggable' target due to its high affinity for GTP and unique protein structure[29,30]. Recent advances in targeting KRAS^{G12C} have led to opportunities for small molecule inhibitors to target wild-type KRAS and other KRAS mutants[31]. MRTX0902 is an orally active and potent KRAS inhibitor that targets SOS1-mediated nucleotide exchange, and is currently undergoing a phase I/II clinical trial (NCT05578092) in combination with adagrasib (MRTX849) for the treatment of solid tumours[32]. Combination treatment with MRTX0902 showed anti-tumour effects with satisfactory pharmacokinetic properties in non-small cell lung cancer (NSCLC) and pancreatic adenocarcinoma (PAAD) mouse xenograft models[33]. In our study, a single-

Fig. 4 | KRAS overexpression suppresses dendritic cell and T-cell recruitment in *c-MYC-lucOS^{OE}/Tp53^{KO}* model. a Quantification of normalised luciferase signals of normal liver (Naïve), *c-MYC-lucOS^{OE}/Tp53^{KO}/EV* (EV) and *c-MYC-lucOS^{OE}/Tp53^{KO}/Kras* (Kras) mice in the first two weeks post-HTVI (one-way ANOVA). Flow cytometry detection of tumour-infiltrating (CD45$^+$TCR-b$^+$CD8$^+$H-2Kb-SIINFEKL$^+$) SIINFEKL-specific CD8$^+$ T cells in livers of both EV and *Kras*-overexpressing mice at week 2 post-HTVI (one-way ANOVA). **b**, **c** Immune profiling by flow cytometry in Naïve, EV and Kras livers. Representative FACs plots of (CD45$^+$CD11c$^+$MHC-II$^+$) DCs and SIINFEKL-specific CD8$^+$ T cells. Quantification showing significant reductions in DCs, (CD45$^+$TCR-b$^+$) total T cells, (CD45$^+$TCR-b$^+$CD8$^+$) CD8$^+$ T cells and SIINFEKL-specific CD8$^+$ T cells in Kras livers (one-way ANOVA). Naïve: $n = 6$ mice, EV: $n = 13$ mice and Kras: $n = 12$ mice examined over 2 independent experiments. **d** Chemokine expression profile demonstrating upregulated *Ccl3* and downregulated *Ccl5*, *Cxcl9*, and *Cxcl11* expressions in Kras livers compared to EV control. RT-qPCR revealed downregulated expression of IFN-associated genes in Kras tumours (two-sided unpaired *t* test). $n = 6$ biologically independent samples/group. Data are presented as mean ± SD. * $p < 0.05$, ** $p < 0.01$, *** $p < 0.001$, **** $p < 0.0001$, n.s. = not significant. Source data are provided as a Source Data file.

dose intravenous dose of MRTX0902 (3 mg/kg) significantly reduced pERK1/2 level to half of that in unresponded anti-PD-1 treated *c-MYC-luc^{OE}/Tp53^{KO}* tumours (Supplementary Fig. 13c), demonstrating potent pathway inhibition. Based on this mechanistic validation, we developed a combinatorial regimen in the *c-MYC-lucOS^{OE}/Tp53^{KO}/Kras* HCC model. *c-MYC-lucOS^{OE}/Tp53^{KO}/Kras* HCC mice were administered a two-week treatment of MRTX0902 (5 mg/kg *q.d.*) coupled with Trametinib (0.2 mg/kg *b.i.d.*) and anti-PD-1 (200 µg *t.i.w.*) (Fig. 7c). Consistent with our hypothesis, *c-MYC-lucOS^{OE}/Tp53^{KO}/Kras* tumours were not responsive to anti-PD-1 treatment, proving that wild-type KRAS activation promotes resistance to immunotherapy in our model (Fig. 7d). Interestingly, the MRTX0902 + PD-1 group shows improved survival compared to the MRTX0902 + IgG-treated group. This finding suggested that MRTX0902 sensitises tumours to anti-PD-1 treatment, conferring a survival benefit. The Trametinib + PD-1 and combo (Trametinib +MRTX0902 + PD-1) group also exhibits reduced luciferase signals and improved survival. Significant suppression of pERK1/2 levels and enhanced CD8$^+$ T cell infiltration was observed upon MRTX0902 and Trametinib treatments, confirming that targeting KRAS signalling increases the therapeutic efficacy of anti-PD-1 therapy (Fig. 7e,f).

Discussion

We identified wild-type KRAS signalling as one of the crucial oncogenic pathways that drive immune evasion in an antigen-expressing *c-MYC-lucOS^{OE}/Tp53^{KO}* mouse model. This model was previously developed by Ruiz de Galarreta et al. to elicit a TAA-specific anti-CD8 T cell response upon recognition of *C-MYC*-tagged exogenous antigens[12]. They highlighted the activation of β-catenin signalling as the major driver for CCL5-mediated immune evasion in HCC. In addition to β-catenin, we demonstrated that wild-type KRAS was elevated in immune-escaped *c-MYC-lucOS^{OE}/Tp53^{KO}* tumours, with the activation of EGFR/MEK/ERK signalling. While a potential interaction between RAS-ERK and β-catenin signalling has been suggested[34], our model and clinical data indicate that overexpression of wild-type KRAS leads to an increase in β-catenin expression, yet the MEK knockout did not alter the β-catenin levels (Supplementary Fig. 15). Mechanistically, activation of wild-type KRAS signalling requires the activation of upstream RTKs, which can be mediated by a TIME rich in cytokines and growth factors[35]. IHC analysis further confirmed that EGF, derived from the infiltrating CD11c$^+$ dendritic cells, was upregulated in the antigen-expressing *c-MYC-lucOS^{OE}/Tp53^{KO}* models. Our findings indicate that KRAS drives immune evasion through suppressing intrinsic and extrinsic interferon signalling pathways via EGFR/MEK/ERK activation, potentially independent of β-catenin signalling.

The role of KRAS in HCC remains largely unexplored due to its low mutation rate in HCC. Indeed, increasing evidence shows that wild-type KRAS expression and its signalling pathway is actively regulated via microproteins, ubiquitination, miRNAs in HCC, contributing to tumorigenesis and therapy resistance independent of mutation status[36–39]. Wild-type KRAS overexpression (14–19% frequency in HCC) was correlated with high tumour recurrence risk and poor patient survival. In terms of molecular classification, HCC with activated RAS/ERK signalling is classified as a proliferative subset[40]. Likewise, wild-type *Kras* in the *c-MYC-lucOS^{OE}/Tp53^{KO}* HCC tumours also confirmed the pro-tumorigenic and proliferative properties of KRAS. Our clinical data are in line with those of Dietrich et al., who reported the overexpression of wild-type KRAS in HCC[36].

While KRAS mutations are well-established drivers of immune evasion across multiple cancer types[41–43], our study reveals that wild-type KRAS activation similarly shapes an immunosuppressive tumour microenvironment in HCC. Mutant KRAS has been reported to promote myeloid immunosuppression in lung and pancreatic cancers[44,45], nonetheless, we also observed an increased infiltration of myeloid cells, including monocytes, macrophages, and neutrophils via CCL3-mediated recruitment, in wild-type KRAS-overexpressing HCC tumours. These innate immune cells exhibit impaired anti-tumour activity and fail to elicit T cell chemotaxis, due to dysregulated inflammatory functions including TNF/NF-κB signalling and interferon (IFN) responses. Based on these findings, these cells may also contribute to immune suppression in addition to impairing intrinsic and extrinsic IFN signalling.

Our findings reveal that wild-type KRAS suppresses both type I and type II IFN responses in HCC, evidenced by decreased expression of IFN-associated genes (*Stat1*, *Stat2*, *Irf1*, *Irf2*, and *Irf9)* and the loss of IFN-stimulated (*Ifit3$^+$Ifit1$^+$Isg15$^+$*) CD8$^+$ T cell populations. Consistent with prior studies[25,46–48], wild type KRAS-mediated suppression of the IFN responses, leads to dysfunctional antigen presentation[44] and a decrease in chemoattractants *Ccl5*, *Cxcl9*, and *Cxcl11* expression. KRAS has also been reported to suppress STING activation via MEK/ERK hyperactivation and subsequently downregulate the expression of chemokines CCL5 and CXCL10[49], which are essential for establishing a T cell-inflamed microenvironment[50]. The deficiency in antigen presentation and T cell chemotaxis collectively disrupts T cell priming and fails to recruit SIINFEKL-specific CD8$^+$ T cells to the tumour site, ultimately leading to the failure of immunosurveillance. With regard to tumour cells, we revealed that wild-type KRAS drives MHC-I downregulation via suppressing intrinsic IFN signalling. These findings are in line with the observation that oncogenic KRAS suppresses the expression of STAT1 and STAT2[51], which are pivotal to regulate the expression of IFN-γ and MHC molecules, T cell infiltration and exhaustion[52]. Our findings highlight that KRAS activation, irrespective of its mutation status, drives immune escape through suppressing the IFN responses and creates a myeloid-rich immunosuppressive TIME, characterised with: DC dysfunction, disruption of T cell recruitment and activation, and dysregulation of MHC-I expression of tumour cells. Importantly, these experimental findings were corroborated by clinical observations showing a significant negative correlation between wild-type KRAS expression levels and CD8 T cell signature, as well as MHC-I expression in human HCC. This triad of immunosuppressive mechanisms provides a molecular explanation for the immunotherapy resistance observed in KRAS-driven HCC.

Strikingly, activation of the KRAS signalling pathway is consistently observed in HCC patients refractory to either anti-PD-1[25] or anti-PD-L1[27] antibodies in two different clinical trials. Furthermore, KRAS activation correlates with a trend toward poorer overall survival in HCC patients receiving the combination of atezolizumab and bevacizumab, although this finding does not reach statistical significance. In our *Kras*-driven immune-escaped HCC model, we demonstrate enhanced therapeutic efficacy of an anti-PD-1 antibody

https://doi.org/10.1038/s41467-025-64860-7

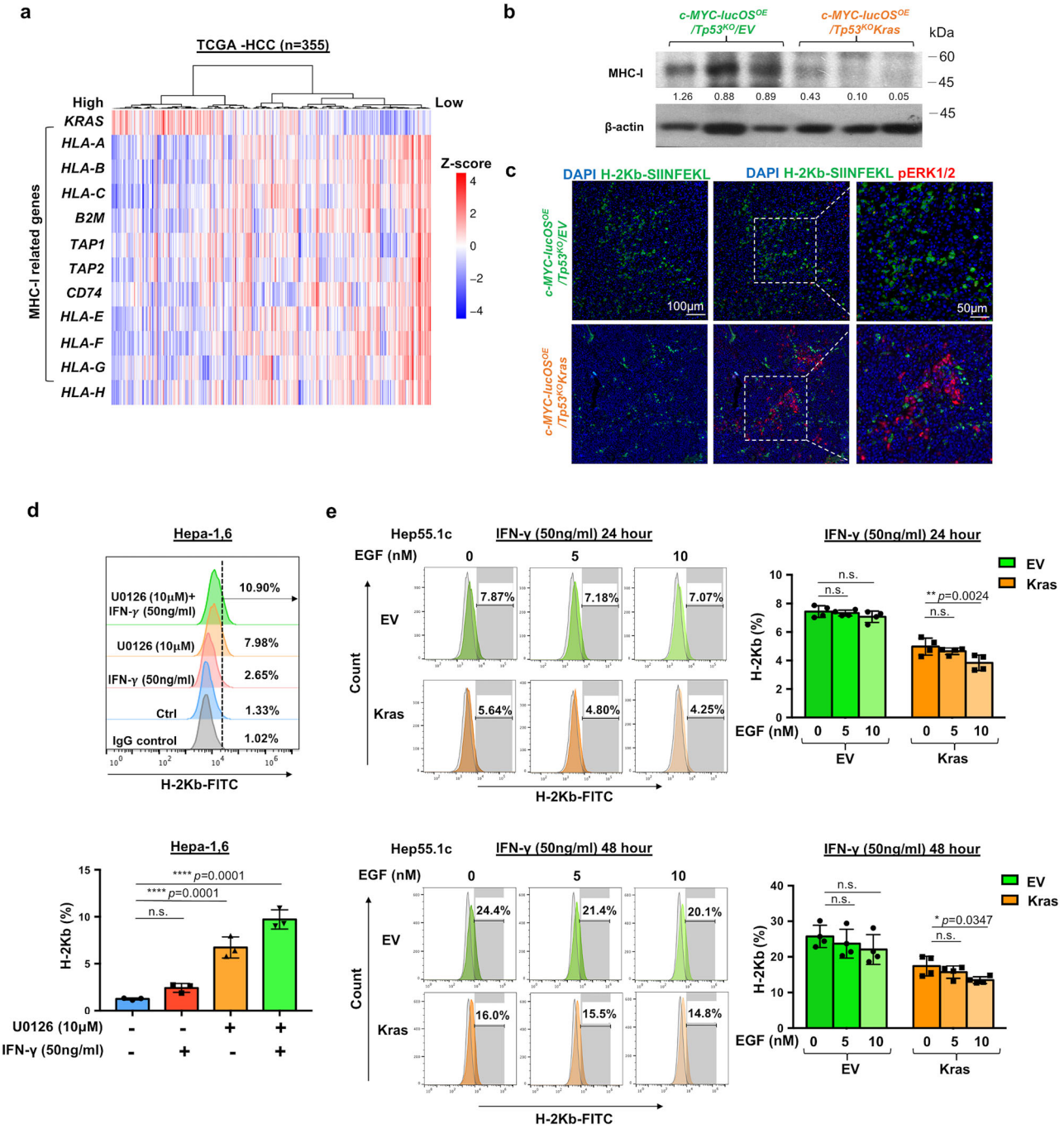

Fig. 5 | Wild-type KRAS suppresses MHC-I antigen presentation through ERK-dependent signalling. a Heatmap of the TCGA-HCC dataset ($n = 355$ patients) showing inverse correlation between KRAS expression and antigen presentation machinery (APM) genes. **b** Western blot demonstrates downregulated MHC-I expression in *c-MYC-lucOS^{OE}/Tp53^{KO}/Kras* tumours compared to *c-MYC-lucOS^{OE}/Tp53^{KO}/EV* tumours. **c** Multiplex IF demonstrates decreased H-2Kb-SIINFEKL (green) and pERK1/2 (red) in *c-MYC-lucOS^{OE}/Tp53^{KO}/EV* and *c-MYC-lucOS^{OE}/Tp53^{KO}/Kras* tumours ($n = 5$ biologically independent samples/ group over 1 independent experiment). Scale bar = 50 μm, 100 μm. **d** Pharmacological inhibition of ERK1/2 (U0126, 10 μM) for 24 h elevates basal and IFN-γ-induced (50 ng/ml) H-2Kb surface expression of Hepa-1,6 mouse HCC cell line (one-way ANOVA). $n = 3$ independent experiments. **e** Flow cytometry analysis shows Kras overexpression (Kras) in Hep55.1c cells dose-dependently attenuates IFN-γ-induced (50 ng/ml) H-2Kb surface expression during EGF treatment (5 and 10 nM) compared to EV control for 24 and 48 hours (two-way ANOVA). $n = 4$ independent experiments. Data are presented as mean ± SD. * $p < 0.05$, ** $p < 0.01$, **** $p < 0.0001$, n.s. = not significant. Source data are provided as a Source Data file.

combined with MRTX0902 and Trametinib targeting KRAS activation compared to an anti-PD-1 antibody alone. Nevertheless, in our study of single-agent MRTX0902 treatment, we observed only a minimal tumour suppressive effect, which is not as pronounced as the effects seen with MEK1/2 knockout. The limited efficacy of MRTX0902 can be attributed to its short half-life, ranging from 0.62 to 1.3 h, as indicated by its comparatively lower efficiency in suppressing pERK1/2 levels when compared to Trametinib. While administering MRTX0902 twice daily could enhance its effects[32], this approach poses logistical challenges; therefore, we opted for once-daily administration instead. As a result, MRTX0902 demonstrates a less potent effect on tumour growth suppression

https://doi.org/10.1038/s41467-025-64860-7

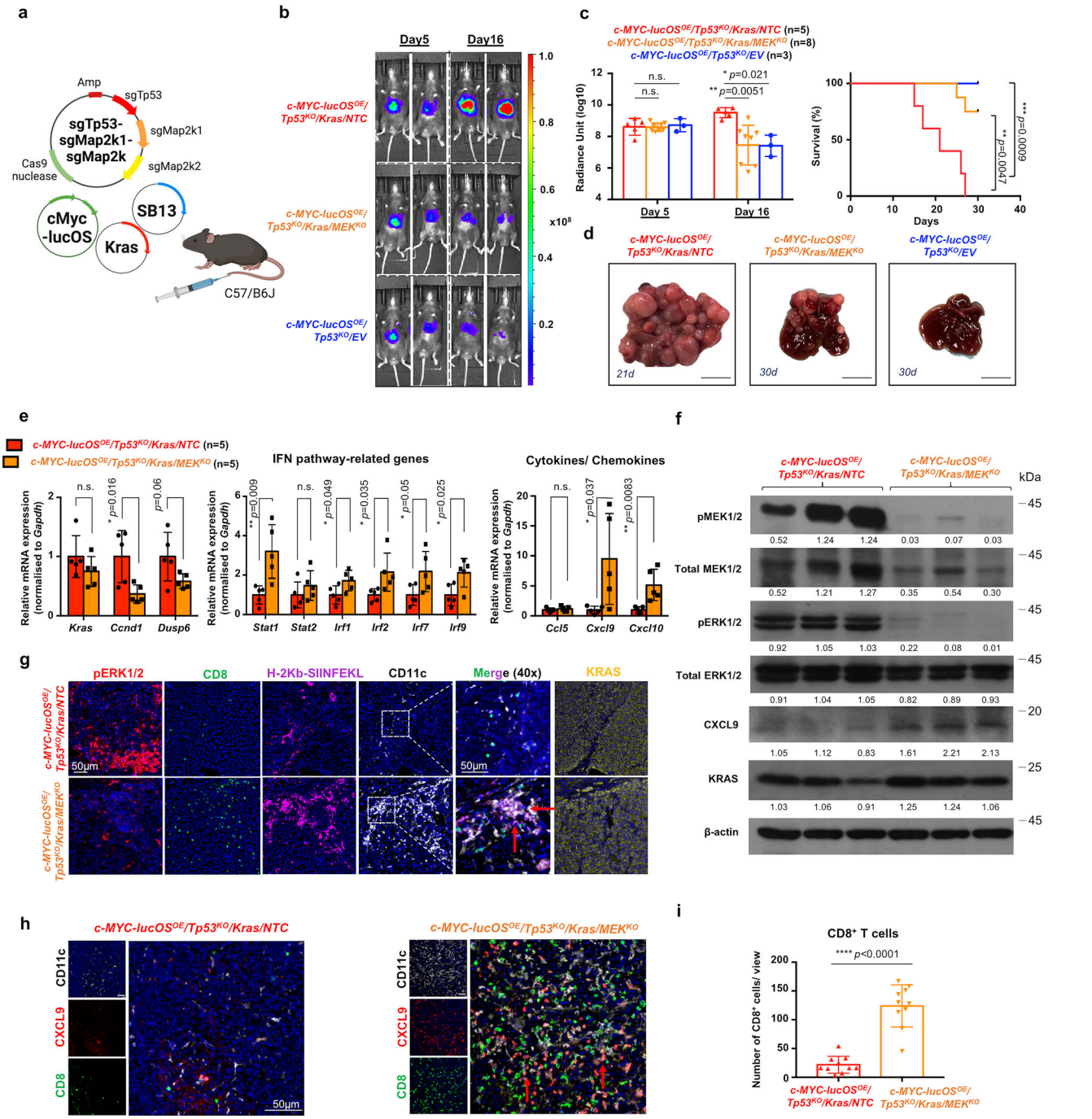

Fig. 6 | In vivo CRISPR/Cas9-mediated MEK1/2 knockout rescues the immunosuppressive effects of wild-type *Kras* overexpression in the *c-MYC-lucOS^{OE}/Tp53^{KO}/Kras* HCC mouse model. a Schematic of CRISPR/Cas9-mediated MEK1/2 knockout in the *c-MYC-lucOS^{OE}/Tp53^{KO}/Kras* HCC mouse model. **b** Representative bioluminescence images and **c** quantification of normalised luciferase signal of *c-MYC-lucOS^{OE}/Tp53^{KO}/Kras/NTC*, *c-MYC-lucOS^{OE}/Tp53^{KO}/Kras/MEK^{KO}* and *c-MYC-lucOS^{OE}/Tp53^{KO}/EV* mice at day 5 and day 16 post-HTVI (one-way ANOVA). Survival analysis (log-rank Mantel–Cox test). **d** Liver images of *c-MYC-lucOS^{OE}/Tp53^{KO}/Kras/NTC*, *c-MYC-lucOS^{OE}/Tp53^{KO}/Kras/MEK^{KO}* and *c-MYC-lucOS^{OE}/Tp53^{KO}/EV* mice. Scale bar = 1 cm. *c-MYC-lucOS^{OE}/Tp53^{KO}/Kras/NTC*: $n = 5$ mice, *c-MYC-lucOS^{OE}/Tp53^{KO}/Kras/MEK^{KO}*: $n = 8$ mice, *c-MYC-lucOS^{OE}/Tp53^{KO}/EV*: $n = 3$ mice examined over 2 independent experiments. **e** RT-qPCR ($n = 5$ biologically independent samples/ group; two-sided unpaired *t* test) and **f** western blot analyses confirmed successful MEK1/2 knockout and reduced pERK1/2, and the downstream pathway-associated genes *Ccnd1* and *Dusp6* upon MEK1/2 knockout. The IFN-inducible genes and chemokines were restored upon MEK1/2 knockout in *c-MYC-lucOS^{OE}/Tp53^{KO}/Kras* livers compared to NTC. **g** Multiplex IHC images compares pERK1/2 (red), CD8 (green), H-2Kb-SIINFEKL (magenta), CD11c (white), and KRAS (yellow) in immune infiltrates of the *c-MYC-lucOS^{OE}/Tp53^{KO}/Kras/NTC* and *c-MYC-lucOS^{OE}/Tp53^{KO}/Kras/MEK^{KO}* tumours. Red arrows indicate H-2Kb-SIINFEKL and CD11c colocalization ($n = 5$ biologically independent samples/ group over 1 independent experiment). Scale bar = 50 μm. **h** Multiplex IHC confirms increased CXCL9^{+} (red), CD11c^{+} DC recruitment (white), and CD8 T cell (green) infiltrates in *c-MYC-lucOS^{OE}/Tp53^{KO}/Kras/MEK^{KO}* tumours. Red arrows indicate CXCL9 and CD11c colocalization ($n = 5$ biologically independent samples/ group over 1 independent experiment). Scale bar = 50 μm. **i** Quantification demonstrates significant increase in tumour-infiltrating CD8^{+} T cells in *c-MYC-lucOS^{OE}/Tp53^{KO}/Kras/MEK^{KO}* tumours versus NTC ($n = 10$ randomly selected views/ groups; two-sided unpaired *t* test). Data are presented as mean ± SD. * $p < 0.05$, ** $p < 0.01$, *** $p < 0.001$,**** $p < 0.0001$, n.s. = not significant. Source data are provided as a Source Data file. The diagram **a** was created using BioRender and included with permission for publication (Created in BioRender. Lee, T. (2025) https://BioRender.com/qnek1je).

https://doi.org/10.1038/s41467-025-64860-7

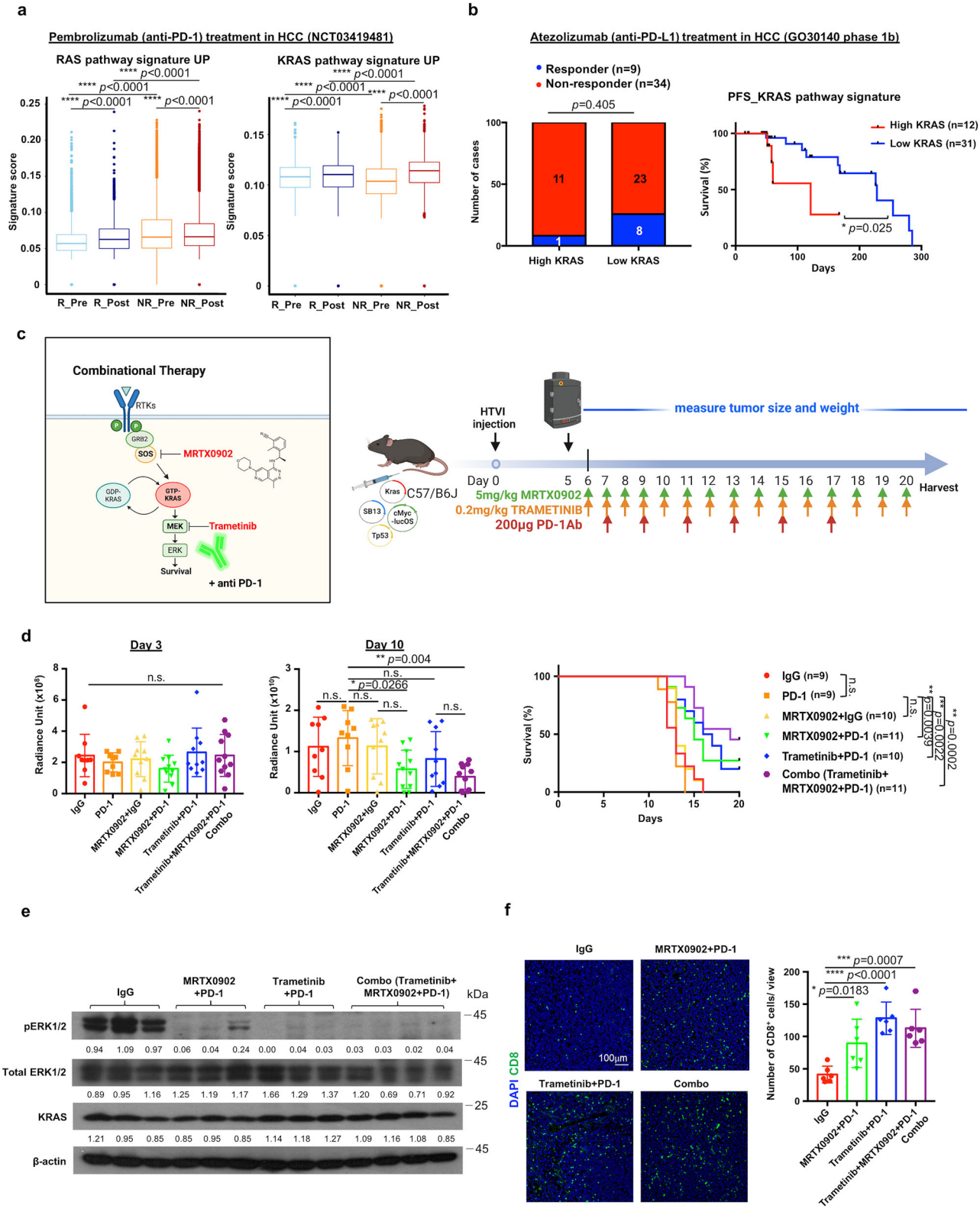

compared to the stable deletion of MEK1/2 achieved through genetic knockout. This limitation is why we included Trametinib in our combination study to ensure effective suppression of pERK1/2, addressing both the short half-life of MRTX0902 and potential pathway reactivation. Nonetheless, combination treatment comprising MRTX092, Trametinib, and PD-1 promoted $CD8^+$ T cell-mediated anti-tumour immunity and increased the sensitivity to immunotherapy. This shed the potential clinical application of combined vertical inhibition of KRAS/ERK signalling using Trametinib and MRTX0902 to synergise with anti-PD-1 treatment.

In conclusion, our study highlights that wild-type KRAS plays a role in driving immune evasion via the suppression of IFN signalling and MHC-I antigen presentation and contributes to resistance to anti-PD-1 therapy (Supplementary Fig. 16). Combined targeting of KRAS/ERK signalling with PD-1 inhibition may be a novel therapeutic strategy for HCC treatment.

Fig. 7 | KRAS signalling drives ICI resistance and the combined effect of MRTX0902, Trametinib, and anti-PD-1 therapy enhances anti-tumour immunity in *c-MYC-lucOS^{OE}/Tp53^{KO}/Kras* mice. a scRNA-seq of HCC biopsies (NCT03419481) reveals elevated baseline RAS/KRAS pathway scores in tumour cells of non-responders ($n = 21$) versus responders ($n = 5$) to pembrolizumab (anti-PD-1) treatment in a phase II clinical trial. R_Pre = responder before treatment, R_Post = responder after treatment, NR_Pre = non-responder before treatment, NR_Post = non-responder after treatment. (R_Pre: $n = 7123$ cells, R_Post: $n = 6104$ cells, NR_Pre: 57099 cells, NR_Post: 52533 cells; two-sided Wilcoxon rank-sum test). Data are expressed as a range (min to max), median as the centre. Whiskers = extend from the box to the min and max values within 1.5 times the IQR from the quartiles, illustrating data variability. **b** Clinical correlation (GO30140 trial) shows high KRAS signature associates with lower response rate (~ 92%; Fisher's exact test) and worse progression-free survival outcome to atezolizumab (anti-PD-L1; High KRAS: $n = 12$, Low KRAS: $n = 31$; log-rank Mantel–Cox test). **c** Schematic of treatment regimens for the MRTX0902 (5 mg/kg), Trametinib (0.2 mg/kg), anti-PD-1 (200 μg) and combined treatment (combo) groups. **d** Quantification of normalised luciferase signals in *c-MYC-lucOS^{OE}/Tp53^{KO}/Kras* mice at day 3 and day 10 post-HTVI (one-way ANOVA). Survival analysis of *c-MYC-lucOS^{OE}/Tp53^{KO}/Kras* mice after treatment with vehicle, MRTX0902, Trametinib or anti-PD−1 treatment (log-rank Mantel–Cox test). IgG: $n = 9$ mice, PD−1: $n = 9$ mice, MRTX0902 + IgG: $n = 10$ mice, MRTX0902 + PD-1: $n = 11$ mice, Trametinib + PD-1: $n = 10$ mice, Combo: $n = 11$ mice examined over 2 independent experiments. **e** Western blot shows pERK1/2 suppression following MRTX0902 and Trametinib. **f** Multiplex IHC images and quantification of intra-tumoral CD8$^+$ T cells (green) staining for IgG, MRTX0902 + PD-1, Trametnib+PD-1 and combo group tumours ($n = 6$ randomly selected views/ groups, one-way ANOVA). Scale bar = 100 μm. Data are presented as mean ± SD. * $p < 0.05$, ** $p < 0.01$, *** $p < 0.001$,**** $p < 0.0001$, n.s. = not significant. Source data are provided as a Source Data file. The diagram **c** was created using BioRender and included with permission for publication (Created in BioRender. Lee, T. (2025) https://biorender.com/vzx4q0f).

Methods

Mouse models

Six to eight-week-old male C57BL/6 (Strain#: 000664) mice were obtained from The Chinese University of Hong Kong and housed under specific-pathogen-free conditions at the Centralised Animal Facilities (CAF) of The Hong Kong Polytechnic University. All mice were housed with a 12 h light-dark cycle (8:00–20:00 light, 20:00–8:00 dark), with controlled room temperature (23 ± 2 °C) and humidity (30–70%), in groups according to stocking density as recommended. All animal experiments were approved by the Animal Experimentation Ethics Committee of The Hong Kong Polytechnic University and conducted in accordance with institutional guidelines for the Use of Live Animals in Teaching and Research. All animal experiments were approved by the Animal Experimentation Ethics Committee of The Hong Kong Polytechnic University and conducted in accordance with institutional guidelines for the Use of Live Animals in Teaching and Research.

For HTVI models, 15 μg of plasmids pT3-EF1A-c-MYC-luc encoding human *c-MYC* with luciferase expression or pT3-EF1A-c-MYC-lucOS encoding *c-MYC* with exogenous antigens and 15 μg CRISPR/Cas9 vector expressing sg*Tp53* (px330-sgTp53) along with 2.5 μg SB13 transposase expressing vector (CMV-SB13) in a ratio of 25:1 were diluted in saline (in a volume ratio 10% of the mouse weight) and injected into the lateral tail vein of six to eight-week-old male wild-type C57BL/6 mice within 5-7 seconds. In order to investigate the effect of KRAS in HCC, 2.5 μg of pT3-EF1A-Kras was added to *c-MYC-luc^{OE}/Tp53^{KO}* model while same amount of empty vector pT3-EF1A as control. In order to investigate the effect of KRAS activation in anti-tumour T cell response, 15 μg of pT3-EF1A-Kras was added to the *c-MYC-lucOS^{OE}/Tp53^{KO}* model. In the *c-MYC-lucOS^{OE}/Tp53^{KO}/KrasS17N* and *c-MYC-lucOS^{OE}/Tp53^{KO}/KrasG12D* and control *c-MYC-lucOS^{OE}/Tp53^{KO}/EV* groups, the same amount of pT3-EF1A-KrasS17N, pT2-KrasG12D or empty vector pT3-EF1A was added instead of wild-type *Kras*-expressing plasmid to maintain the consistent transfection efficiency. To assess the effect of MEK inhibition, the px330-sg*Tp53*-sg*Map2k1*-sg*Map2k2* and the same amount of its control px330-sg*Tp53*-sgNTC, were injected into the mice hepatocytes in the combination of pT3-EF1A-Kras, pT3-EF1A-c-MYC-lucOS and CMV-SB13.

The orthotopic NAFLD-HCC model was established as described previously[53]. Briefly, six-to-eight-week-old male C57BL/6 were fed a methionine and choline-deficient (MCD) diet (Research Diet) for two weeks prior to intrahepatic tumour injection. A suspension of RIL-175 cells at a density of 5000 cells were mixed with 50% Matrigel was orthotopically injected into the right lobe of the mouse liver.

To monitor the tumour growth, mice were administered with 100 mg/kg D-luciferin (Gold Biotechnology) via intraperitoneal (IP) injection 5 min before bioluminescent imaging (Perkin-Elmer IVIS Lumina Series III Pre-clinical In Vivo Animal Imaging Systems) at defined time points. Mice were euthanised if the tumour burden exceeded 10% of body weight or if body weight loss was greater than 20%. The maximal tumour size/ burden was permitted by the study protocol of the Hong Kong Polytechnic University. The maximal tumour size/burden was not exceeded in all experiments. Mice were euthanised by cervical dislocation under anaesthesia by trained and experienced staff. The study protocol was approved by and performed in accordance with the Committee of the Use of Live Animals in Teaching and Research at the Hong Kong Polytechnic University (Hong Kong, P.R. China).

Plasmids

pT3-EF1A-c-MYC-lucOS was a gift from Dr. Amaia Lujambio (Addgene plasmid #129776; http://n2t.net/addgene:129776; RRID:Addgene_129776). pT2-KrasG12D was a gift from Dr. Weonsang Simon Ro[54]. With regards to *Kras* overexpression constructs: pT3-EF1A-Kras (5698 bp): Mouse *Kras* (NM_021284) was cloned into pDONR-221 (Hitrobio Biotechnology) and transferred to pT3-EF1A vector via Gateway LR Clonase (Thermo Fisher Scientific). pT3-EF1A-KrasS17N was generated by site-directed mutagenesis (Ser17→Asn; AGC → AAC) (GenScript Biotech). For in vivo MEK1/2 knockout, the px330-sgTp53-sgMap2k1-sgMap2k2 (9373 bp) was composed by Genscript Biotech. The single guide RNAs (sgRNAs) targeting mouse MEK1 (sg*Map2k1*:-CATTCTAGTGAACTCACGTG) and MEK2 (sg*Map2k2*: GTGCAACTCGCCCTACATCG) referenced from Mouse CRISPR Knockout Pooled Library (Brie) were cloned into the CRISPR/Cas9 vector expressing sg*Tp53* (px330-sgTp53). For the control plasmid, a non-targeting control (sgNTC: GAAACACCGGGTCTTCGAGAAGACCT) was used. For the wild-type *Kras* overexpression in a murine HCC cell line, the lentivirus expressing wild-type *Kras* pLVX-flag-Kras-Puro (mouse Kras, NM_021284) packaged by WZ Biosciences Inc.

Cell lines and cell culture

The murine HCC cell lines Hep55.1c, Hepa-1,6 and RIL-175 were maintained in complete DMEM or RPMI (DMEM or RPMI 1640 medium supplemented with 10% heat-inactivated FBS and 1% penicillin-streptomycin) at 37 °C in a humidified chamber containing 5% CO_2. Wild-type *Kras* overexpressing Hep55.1c cell line was generated through lentiviral transfection of pLVX-flag-Kras-Puro and maintained in DMEM containing puromycin (2 μg/mL). The culture medium was refreshed every two days. All cell lines used in this study were obtained between 2013 and 2016, and they were regularly authenticated by morphological observation and AuthentiFiler STR (Invitrogen) as well as tested for the absence of mycoplasma contamination (mycoAlert, Lonza). Cells were used within 20 passages after thawing.

Tumour-infiltrating immune cell isolation and purification

Tumour tissues of HTVI mice were dissociated in a dissociation buffer containing 0.5 mg/ml

Collagenase IV (Invitrogen) and 0.1 mg/ml DNaseI (Roche), using the gentleMACS dissociator (Miltenyi Biotec) at 37 °C. Single cell suspensions was filtered with a 70μm cell strainer and centrifuged at 600 × *g* for 10 min. Immune cells were then enriched via a density-gradient centrifugation approach using Percoll PLUS (Cytvia) at 1200 × *g* for 25 min at 20 °C with no brake. After centrifugation, the immune cell layer was transferred to a new tube and treated with ACK lysing buffer (Gibco) to remove red blood cells. The suspension was centrifuged at 700 × *g* for 5 min, and the pellet was resuspended in complete RPMI medium.

Sample preparation and liquid chromatography with tandem mass spectrometry (LC-MS/MS) data acquisition

Mouse tumour samples were homogenised and extracted using Easy-Pep MS Sample Prep Kits (Thermo Fisher Scientific) according to the manufacturer's instructions. The peptide samples were dried using Refrigerated CentriVap Vacuum Concentrators with Cold Traps (Labconco) and resuspended in 100 ml of 0.1% formic acid (FA) in water for LC-MS/MS analysis.

LC-MS/MS analyses were performed on an Orbitrap Fusion Lumos Tribrid Mass Spectrometer (Thermo Fisher Scientific) coupled with UltiMate 3000 RSLCnano System (Thermo Fisher Scientific). A 1 mm × 5 mm trap cartridge and a C18 analytical column (75 µm × 250 mm, 2 µm, 100 Å) (Acclaim PepMap, ThermoFisher Scientific, USA) were employed for heat-trapping and LC separation, respectively. Mobile phases A and B consisted of 0.1% FA in water and 0.1% FA in 100% Acetonitrile (ACN), respectively. Peptides were first trapped for 10 min with 100% A with a flow rate of 10 ml/min, followed by separation with a flow rate of 300 nL/minute: mobile phase B at 2% in 0–10 min (trapping time), 2-6% in 10–12 min; 6–20% in 12–82 min 20–30% in 82–92 min, 30–90% in 92–100 min and held until 105 min, and returned to 2% at 105 min and maintained until 120 min. Both trapping and LC separation were performed in a column oven maintained at 50 °C.

Data were collected separately in modes of data-dependent acquisition (DDA) and DIA-MS. The spray voltage and ion transfer tube temperature were maintained at 2300 V and 300 °C, respectively, throughout all acquisitions. In both acquisition modes, an MS scan with an m/z range of 400–1500 was performed with an Orbitrap resolution of 60,000 maximum injection time of 20 milliseconds and a standard AGC target. In DDA mode, precursors with charge states 2-7 were selected for MS/MS analysis with a normalised high collision dissociation energy of 30%. Dynamic exclusion time was set as 40 s. Data-dependent MS/MS spectra were acquired using the orbitrap analyser with a resolution of 7500 maximum injection target of 30 milliseconds, and standard AGC target. The cycling time of each DDA cycle was set to be 3 s. In DIA mode, the precursor was fragmented using HCD energy of 32%. The isolation window was set to be 20 m/z in a 400–1500 precursor range, i.e., in a total of 55 scan events in each cycle. MS/MS spectra were acquired using an Orbitrap analyser with a resolution of 30,000 scan range of 200–2000 m/z, and maximum injection time of 50 ms.

DIA-MS data analysis

The acquired label-free DDA data from *c-MYC-luc*^{OE}*/Tp53*^{KO} HCC and *c-MYC-lucOS*^{OE}*/Tp53*^{KO} HCC samples (n = 5/group) were processed in Spectronaut (v17, Biognosys) to generate a spectral library for subsequent data-independent acquisition (DIA) quantification. DIA data were analysed using the mouse UniProt database (release 2022_01, 23 Feb 2022) with default BGS Factory Settings. In parallel, the same DDA data were analysed in Progenesis QI for Proteomics (Waters Corp.) using Mascot Server 2.4 (Matrix Science) for protein identification. The precursor ion mass tolerance and fragmentation tolerance were set as 10 ppm and 0.05 Da for the database search, respectively. The maximum number of modifications per peptide was three. Carbamidomethylation of cysteine was set as a fixed modification, and oxidation of methionine and N-terminal acetylation were set as variable modifications. The enzyme was specified as trypsin with up to two missed cleavages allowed. The false discovery rate for peptide matches and proteins was adjusted to 1%.

In Spectronaut, protein identifications (UniProt accessions) were automatically mapped to gene symbols and Gene Ontology IDs (GOIDs) using annotations from the UniProt database during the database search and quantification workflow. The mouse UniProt database (release 2022_01) contains pre-annotated gene identifiers (e.g., gene symbols, Ensembl IDs) and Gene Ontology (GO) terms for each protein entry.

For pathway analysis, the log2 ratio of identified genes (*c-MYC-lucOS*^{OE}*/Tp53*^{KO} versus *c-MYC-luc*^{OE}*/Tp53*^{KO} samples; n = 5/group) were analysed in Gene Set Enrichment Analysis (GSEA) software_4.2.3. The (MSigDB mouse) MH: hallmark gene sets, GOBP: Biological Processes subset of GO Gene Ontology, and CGP: chemical and genetic perturbations databases were used. Significantly enriched pathways were defined as those with a nominal $p < 0.05$.

Single-cell RNA sequencing (scRNA-seq) and processing

Total immune cells from HTVI-induced *c-MYC-lucOS*^{OE}*/Tp53*^{KO}*/EV* and *c-MYC-lucOS*^{OE}*/Tp53*^{KO}*/Kras* tumours were purified and stained with anti-CD45-APC antibody (#55984, BD Biosciences) for 45 minutes on ice. LIVE/DEAD Fixable Near-IR Dead Cell Stain Kit (Thermo Scientific) was used for the exclusion of dead cells. The live CD45$^+$ cells was sorted on BD FACSAriaIII cell sorter (BD Biosciences), cells from 3 mice per group were pooled into one sample. Sorted cells were immediately processed for single-cell encapsulation and barcoding using the Chromium Next GEM 3' v3 Chemistry Single-Cell Kit (10X Genomics). Libraries were prepared and sequenced on an Illumina NovaSeq platform at the Beijing Genomics Institute.

Initial data demultiplexing, read alignment, UMI counting, and annotation of the raw read data were performed using the Cell Ranger Single-Cell software v9 (10X Genomics). Raw sequencing reads of the two samples (EV and Kras) were mapped to the mouse genome (mm10). Data from both samples (EV and Kras) were merged and analysed in Seurat v5.3.0 (R package). Low-quality or dying cells with low sequencing depth, low genetic content, or mitochondrial contamination were filtered out based on quality control metrics. For quality control, cells with < 200 unique genes detected or > 10% mitochondrial reads were excluded. Major immune cell clusters were visualised using UMAP and annotated using published marker genes.

Sequencing data HRA001748 from human HCC patients was retrieved from BioProject (https://ngdc.cncb.ac.cn/bioproject/browse/PRJCA007744)[22]. Patients with less than 50 cells in the HCC tumour population were excluded. 71 human HCC samples were stratified into 'High KRAS' (n = 10) and 'Low KRAS' (n = 61) groups based on tumour cell KRAS expression levels (threshold: top 14% expression matching TCGA-HCC KRAS overexpression frequency). Total immune cell numbers were balanced (n = 32718 cells/ group) through random subsampling of the 'Low KRAS' group for subsequent analysis.

In vivo combinational therapy of MRTX0902, trametinib and anti-PD-1 antibodies

The *c-MYC-lucOS*^{OE}*/Tp53*^{KO}*/Kras* HCC mouse model was induced in C57BL/6 mice via HTVI, as described previously. The two-week treatment commenced on day 6 after HTVI. The mice were administered the SOS1 inhibitor MRTX0902 (5 mg/kg *q.d.*, MedChemExpress) via intravenous (IV) injection, coupled with a daily oral administration of trametinib (0.2 mg/kg *b.i.d.*, MedChemExpress), and anti-PD-1 (200 µg *t.i.w.*, #BE0146, Bio X Cell) through IP injection. Tumour growth was monitored using bioluminescence imaging at

specific time points. The tumour tissues were harvested for gene and protein expression analyses.

In vitro *drug treatment*

HCC cells were seeded in six-well plates at a density of 1×10^3–5×10^3 cells/well and allowed to adhere for 24 h. To induce MHC-I (H-2Kb) expression, cells were treated with IFN-γ (50 ng/mL). Subsequently, the following treatments were applied ERK inhibitor U0126 (10 μM) or EGF (5 nM or 10 nM). Cells were incubated for 24 or 48 h, harvested, and analysed by flow cytometry to assess changes in MHC-I expression.

Flow cytometry

Total immune cells from HTVI-induced *c-MYC-lucOS^{OE}/Tp53^{KO}/EV, c-MYC-lucOS^{OE}/Tp53^{KO}/Kras* and naïve livers were dissociated into single cell suspensions and exclude the dead cells using Zombie Aqua Fixable Viability Kit (1:200; BioLegend, 423101) according to the manufacturer's instructions. Cells were blocked with TruStain FcX anti-mouse CD16/CD32 (BioLegend) and stained with fluorophore-conjugated antibodies for 30 min at 4 °C. For intracellular staining, the cells were then fixed and permeabilised using eBioscience Foxp3/Transcription Factor Staining Buffer Set (#00-5523-00, Invitrogen) according to the manufacturer's instructions. Cells were stained with intracellular antibodies for 30 minutes at 4 °C after fixation, and washed with 1X Permeabilization Buffer. The stained cells were resuspended in FACS buffer (1x PBS supplemented with 0.1% BSA, 2 mM EDTA, and 0.09% sodium azide) and analysed by BD LSRFortessa Cell Analyser. The antibodies used for flow cytometry were anti-mouse CD3 (clone 145-2C11) (1:100, BioLegend, 100355), CD4 (clone GK1.5) (1:300, BioLegend, 100433), CD8a (clone 53-6.7) (1:100, BioLegend, 100737), CD11b (clone M1/70) (1:300, BioLegend, 101205), CD11c (clone N418) (1:200, BioLegend, 117309), CD19 (clone 6D5) (1:100, BioLegend, 115541), CD44 (clone IM7) (1:300, BioLegend, 103057), CD45 (clone 30F11) (1:500, BioLegend, 103115), CD49b (clone DX5) (1:100, BioLegend, 108907), F4/80 (clone BM8) (1:50, BioLegend, 123133), Ki67 (clone 16A8) (1:100, BioLegend, 652419), Ly6C (clone HK1.4) (1:700, BioLegend, 128045), Ly6G (clone 1A8) (1:300, BioLegend, 127643), I-A/I-E (clone M5/114.15.2) (1:500, BioLegend, 107629), TCR-beta (clone H57-597) (1:100, BioLegend, 109251) and MHC Class I Pentamers SIINFEKL (1:100, Proimmune, F93-0A-G). Samples were then analysed on BD LSRFortessa cell analyser or BD FACSymphony A3 Cell Analyser (BD Biosciences) with data analysed on Flow Jo v10.4 (BD Biosciences). Gating Strategies were provided in Supplementary Fig. 7a and immune cell populations were defined as in Supplementary Table 3.

For MHC-I (H-2Kb) detection, Hepa1-6 and Hep55.1c cells were stained with anti-H-2Kb antibody (clone AF6-88.5) (1:100, BioLegend, 116505) in PBS containing 2% FBS for 30 minutes at 4 °C. Isotype-matched mouse IgG were used as negative controls. Flow cytometry was performed on a BD Accuri C6 system, with data analysed on Flow Jo v10.4 (BD Biosciences).

Immunohistochemistry (IHC)

Sections were deparaffinised in xylene and rehydrated in graded alcohols and distilled water. Slides were processed for antigen retrieval by a standard microwave heating technique in Tris-EDTA buffer. Endogenous peroxidase activities were quenched using 3% hydrogen peroxide. The sections were immersed in serum-free protein block solution (DAKO). Specimens were subsequently incubated with the primary antibodies c-MYC (1:200, Abcam, ab32072), human KRAS (1:100, LifeSpan BioSciences, LS-B4683), mouse KRAS (1:100, Santa Cruz Biotechnology, sc-30), P53 (1:200, Abcam, ab26), pEGFR (1:100, Cell Signalling Technology, 3777; 1:100, Santa Cruz Biotechnology, sc-81488) and pERK1/2 (1:200, Cell Signalling Technology, 9101) for mouse HCC samples and human HCC tissue microarray. The sections were then washed thoroughly and incubated with anti-rabbit Envision HRP-conjugated secondary antibody (DAKO). Positive signals were visualised using the Liquid DAB + Substrate-Chromogen System (DAKO). Sections were counterstained with Mayer's haematoxylin and examined using a light microscope. For quantitation of KRAS expression in a tissue microarray, the stained sections were assessed with no prior knowledge of the clinicopathological data for the patients. For intensity (I), each specimen was individually scored from 0 to 1, 0 represents weak and belongs to the 'low expression' group; while 1 represents strong and belongs to the 'high expression'.

Multiplex IHC

The tyramide signal amplification-based method was used for staining multiple targets in HCC paraffin-embedding specimens with Opal 4-Colour Manual IHC Kit (#NEL810001KT, Akoya Biosciences). Sections were deparaffinised in xylene and rehydrated in decreasing graded alcohols and distilled water. Slides were processed for antigen retrieval by a standard microwave heating technique in 1X AR9 Tris-EDTA buffer (pH9.0, #AR900250ML, Perkin Elmer) for 15 minutes. Endogenous peroxidase activities were quenched using 3% hydrogen peroxide for 10 min at room temperature. The sections were immersed in the blocking/antibody diluent (#ARD1001EA, Perkin Elmer) for 30 min at room temperature. The specimens were subsequently incubated with the antibodies β-Catenin (1:200, Cell Signalling Technology, 8480), CD4 (1:500, Cell Signalling Technology, 25229), CD8a (1:500, Cell Signalling Technology, 98941), CD11c (1:200, Cell Signalling Technology, 97585), CK19 (1:5000, Abcam, ab52625), CXCL9 (1:1000, Abcam, ab137792), EGF (1:200, Abcam, MA5-15606), pEGFR (1:100, Cell Signalling Technology,3777), pERK1/2 (Thr202/Tyr204) (1:200, Cell Signalling Technology, 9101), GZMB (1:1000, Cell Signalling Technology, 44153), H-2Kb-SIINFEKL (clone 25-D1.16) (1:100, BioLegend, 141606), HNF4a (1:1000, Abcam, ab201460), HNF1b (1:100, Abcam, ab213149), KRAS (1:100, Santa Cruz Biotechnology, sc-30) and P53 (1:200, Abcam, ab26). The sections were then washed thoroughly and incubated with Opal polymer HRP Ms+Rb for 30 minutes at room temperature. After a brief wash with 1xTBST, Opal 520, 570 and 690 fluorophores (1:100) were applied for 15 min. Staining steps were repeated for each antibody staining. A final stripping step was performed in 1x AR6 sodium citrate buffer (pH 6.0) in a microwave oven for 15 min. The section slides were cooled down and stained with DAPI solution (1:1000). Slides were examined using Nikon Eclipse Ti2-E Live-cell Fluorescence Imaging System (Nikon).

Real-time quantitative PCR (RT-qPCR) analysis

Total RNA from murine samples was extracted using TRIzol Reagent (Invitrogen, Waltham, MA). Samples were lysed for 30 s and paused for 2 min using Precellys Evolution tissue homogeniser and Cryolys cooling (Bertin Technologies). Homogeniser cycles were repeated twice. Chloroform (Merck, Kenilworth, NJ) was added and mixed with a ratio of 1:5 to the volume of TRIzol Reagent. The chloroform-TRIzol mixture was centrifuged at 17000 × *g* for 30 min at 4 °C for phase separation. The top aqueous layer was withdrawn and transferred to a new tube. 500 μl of 100% isopropanol (Merck, Kenilworth, NJ) was added to the aqueous layer and incubated at 4 °C for 20 min for RNA precipitation. After incubation, the solution was centrifuged at 17000 × *g* for 20 min at 4 °C to collect RNA pellets. The supernatant was discarded, and the pellet was washed twice with 1 ml of 75% ethanol (Merck, Kenilworth, NJ) and centrifuged at 11200 × *g* for 15 min at 4 °C. The pellet was air-dried at room temperature and resuspended in UltraPure distilled water (Invitrogen, Waltham, MA). RNA concentration was measured with NanoDrop One/One^C Microvolume UV-Vis Spectrophotometer (Thermo Scientific) and kept at − 80 °C for long-term storage. cDNA was synthesised using the PrimeScript RT Reagent Kit (Takara) according to the manufacturer's instructions. The mixture was incubated at 37 °C for 15 min, followed by 85 °C for 5 s for cDNA production. The cDNA was diluted with UltraPure Distilled Water to make a 10-fold dilution and was stored at − 20 °C. The cDNA samples were mixed

with Bright Green 2X RT-qPCR Master Mix (Applied Biological Materials Inc., Canada) in accordance with the manufacturer's instructions. The PCR analysis was performed using QuantStudio 7 Flex Read Time PCR System (Applied Biosystems) with primers specific to the sequences of genes of interest, which are provided in Supplementary Table 4. Relative expression differences were calculated using $2^{-\Delta\Delta}C_T$ method with reference to housekeeping genes *β-actin* or *Gapdh* or *18S*.

RAS-GTP assay

KRAS activation was examined using Ras Activation Assay Kit (#17-218, Merck Millipore) according to the manufacturer's protocol. Briefly, mouse liver tissues were harvested and lysed with Mg^{2+} lysis buffer supplemented with protease and phosphatase inhibitor cocktails (Roche). The RAS were pulled down using RAS binding domain of RAF-1 (RAF-RBD) bounded glutathione agarose beads. After incubation for three hours at 4 °C with agitation, the beads were pelleted and washed. The agarose beads were resuspended in 2X Laemmli reducing sample buffer and boiled for 10 minutes. Western blotting was performed using anti-KRAS antibody (1:1000, Santa Cruz Biotechnology, sc-30). Endogenous KRAS expression was also examined in the unpulled down lysate as loading control.

Western blotting

Tumour samples were homogenised at 4 °C using Precellys Evolution tissue homogeniser and Cryolys cooling (Bertin Technologies) and extracted using either RIPA buffer supplemented with a protease inhibitor cocktail and phosphatase inhibitors (Roche). Protein lysates were separated by SDS-polyacrylamide gel electrophoresis (SDS-PAGE) and transferred to a polyvinylidene difluoride membrane (Millipore). Membranes were probed with primary antibodies: α-tubulin (1:5000, Merck, T9026), β-actin (1:5000, Millipore Sigma, A5316), β-Catenin (1:2000, Cell Signalling Technology, 8480), CXCL9 (1:1000, Abcam, ab137792), EGF (1:1000, Santa Cruz Biotechnology, sc-374255), pEGFR (1:1000, Santa Cruz Biotechnology, sc-81488), EGFR (1:1000, Santa Cruz Biotechnology, sc-373746), pERK1/2 (Thr202/Tyr204) (1:1000, Cell Signalling Technology, 9101), ERK1/2 (1:1000, Cell Signalling Technology, 9102), KRAS (1:1000, Santa Cruz Biotechnology, sc-30), MHC-I (1:1000, Santa Cruz Biotechnology, sc-59200), pMEK1/2 (Ser217/221) (1:1000, Cell Signalling Technology, 9154), MEK1/2 (1:1000, Cell Signalling Technology, 9122), GZMB (1:1000, Cell Signalling Technology, 44153) overnight at 4 °C. After washing, membranes were incubated with HRP-conjugated secondary antibodies (anti-mouse/rabbit, GE Healthcare) and visualised using enhanced chemiluminescence. Band intensities were quantified using ImageJ software.

The Cancer Genome Atlas (TCGA) data analysis

Clinical, genomic, and transcriptomic data of HCC subtypes were obtained from TCGA-LIHC via the NCI Genomic Data Commons (GDC) using the TCGAbiolinks R package. Fibrolamellar carcinomas, mixed HCC subtypes, and KRAS-mutant samples were filtered out. The RNASeq V2 data was processed and normalised using the RSEM method[55]. Patients were separated based on the z-score of KRAS mRNA expression and categorised into: 'High KRAS': z-score > 1, 'Intermediate KRAS': -1 ≤ z-score ≤ 1, 'Low KRAS': z-score < -1 for downstream analyses, including expression, survival, immune correlation and pathway enrichment analyses. The correlation analyses between the abundance of MHC-I related genes and KRAS expressions across 30 TCGA cancer types were calculated by GSVA using web portal TISIDB[56].

Tissue microarray

51 archived paraffin-embedded pathological specimens from primary HCC patients were collected along with complete clinical and pathological data at the Sun Yat-sen University Cancer Centre. All samples were anonymous. This study was approved by the Institute Research Medical Ethics Committee (G-2022-105-01). Among the 51 samples collected, 47 participants were male, while 4 were female. Median age of the participants was 52. None of the patients had received radiotherapy or chemotherapy before surgery. The clinicopathological features of the patients were described previously[57].

O-link proteomic analysis

The plasma samples of 27 HCC patients upon anti-PD-1 based treatment were collected from Prof. Yin Ying Lu at the Comprehensive Liver Cancer Centre, The Fifth Medical Centre of PLA General Hospital, Beijing, with approval from the Institutional Review Board for ethical review (KY-2021-12-35-1). Plasma proteomic profiling was performed at Immuno Diagnostics Limited (Hong Kong, China) using the multiplex PEA technology. There were 92 biomarkers preselected from the Olink Target 96 Immuno-oncology panel. The oligonucleotide antibody pairs contained unique DNA sequences, allowing hybridisation only to each other. The R package 'Olink Analyse' was used to identify the sets of DEPs between the two groups. Proteins with a p-value of < 0.05 were considered to be differentially expressed.

Calculation of pathway signature score

To assess antigen presentation activity, the ANTIGEN_PROCESSING_AND_PRESENTATION_MACHINERY_SIGNATURE was derived from Thompson et al.[18]. To evaluate enrichment, GSEA was performed using log2FC values from differentially expressed genes between the EV and Kras groups in DC clusters.

To evaluate KRAS pathway activity in HCC patients treated with pembrolizumab (anti-PD-1; NCT03419481[26]), two pathway signatures, RAS pathway signature UP and KRAS pathway signature UP, were established. Gene signature scores were calculated for each tumour cell as the arithmetic mean of the log2 value of expression of all genes in each group.

The information of genes involved in each gene set was listed in Supplementary Table 5.

Reagents

All the reagents used in this study are listed in Supplementary Table 6.

Quantification and statistical analysis

All statistical analyses were performed using GraphPad Prism 7 (GraphPad Software). Data from RT-qPCR, flow cytometry, and mIHC quantification were analysed using an unpaired, two-sided Student's t test between two groups, or ANOVA in comparison with more than two groups. Results are presented as mean, with error bars representing standard deviation (± SD). Outliers (> 3 SD from the mean) were excluded. For CIBERSORT immune composition analysis, the Wilcoxon rank-sum test was implemented. For correlation analyses, Spearman's rank correlation or Fisher's exact test were applied where appropriate. Log-rank Mantel-Cox test survival analysis was used to analyse the disease-free survival and overall survival. Investigators were not blinded to the group allocation during the experiment, and when assessing the outcome in all experiments, including animal experiments. There was no estimate of variation within each group of data. Variance was similar between the compared groups.

Reporting summary

Further information on research design is available in the Nature Portfolio Reporting Summary linked to this article.

Data availability

The scRNA-seq and proteomics data from this study have been deposited in the GEO database under accession code GSE301547 and in the proteomeXchange database under accession code PXD058362. The scRNA-seq data of 26 HCC patient biopsies in the clinical trial on pembrolizumab (NCT03419481) was retrieved from Xiong et al.[26]. The

raw RNA-seq for the GO30140 trial (NCT0271553) was retrieved from the European Genome-Phenome Archive under accession no. EGAS00001005503 through the clinical study data request platform (https://vivli.org/)[28]. Sequencing data HRA001748 from human HCC patients was retrieved from BioProject (https://ngdc.cncb.ac.cn/bioproject/browse/PRJCA007744)[22]. Clinical, genomic, and transcriptomic data of HCC subtypes were obtained from TCGA-LIHC via the NCI Genomic Data Commons (GDC) using the TCGAbiolinks R package. All data are included in the Supplementary Information or available from the authors, as are unique reagents used in this Article. The raw numbers for charts and graphs are available in the Source Data file whenever possible. Source data are provided in this paper.

References

1. Sung, H. et al. Global cancer statistics 2020: GLOBOCAN estimates of incidence and mortality worldwide for 36 cancers in 185 countries. *Ca. Cancer J. Clin.* **71**, 209–249 (2021).
2. Abou-Alfa, G. K. et al. Cabozantinib in patients with advanced and progressing hepatocellular carcinoma. *N. Engl. J. Med.* **379**, 54–63 (2018).
3. Shlomai, A., Leshno, M. & Goldstein, D. A. Regorafenib treatment for patients with hepatocellular carcinoma who progressed on sorafenib—A cost-effectiveness analysis. *PLoS ONE* **13**, 1–11 (2018).
4. Finn, R. S. et al. Atezolizumab plus bevacizumab in unresectable hepatocellular carcinoma. *N. Engl. J. Med.* **382**, 1894–1905 (2020).
5. Kudo, M. et al. Ramucirumab after prior sorafenib in patients with advanced hepatocellular carcinoma and elevated alpha-fetoprotein: Japanese subgroup analysis of the REACH-2 trial. *J. Gastroenterol.* **55**, 627–639 (2020).
6. Abou-Alfa, G. K. et al. Phase 3 randomized, open-label, multicenter study of tremelimumab (T) and durvalumab (D) as first-line therapy in patients (pts) with unresectable hepatocellular carcinoma (uHCC): HIMALAYA. *J. Clin. Oncol.* **40**, https://doi.org/10.1200/JCO.2022.40.4_suppl.379 (2022).
7. El-Khoueiry, A. B. et al. Nivolumab in patients with advanced hepatocellular carcinoma (CheckMate 040): an open-label, noncomparative, phase 1/2 dose escalation and expansion trial. *Lancet* **389**, 2492–2502 (2017).
8. Spranger, S., Bao, R. & Gajewski, T. F. Melanoma-intrinsic β-catenin signalling prevents anti-tumour immunity. *Nature* **523**, 231–235 (2015).
9. Peng, W. et al. Loss of PTEN promotes resistance to T cell–mediated immunotherapy. *Cancer Discov.* **6**, 202–216 (2016).
10. Sia, D. et al. Identification of an immune-specific class of hepatocellular carcinoma, based on molecular features. *Gastroenterology* **153**, 812–826 (2017).
11. Harding, J. J. et al. Prospective genotyping of hepatocellular carcinoma: Clinical implications of next-generation sequencing for matching patients to targeted and immune therapies. *Clin. Cancer Res.* **25**, 2116–2126 (2019).
12. de Galarreta, M. R. et al. -catenin activation promotes immune escape and resistance to anti–PD-1 therapy in hepatocellular carcinoma. *Cancer Discov.* **9**, 1124–1141 (2019).
13. Zhou, J. et al. Hepatoma-intrinsic CCRK inhibition diminishes myeloid-derived suppressor cell immunosuppression and enhances immunecheckpoint blockade efficacy. *Gut* **67**, 931–944 (2018).
14. Chiu, D. K. C. et al. Hypoxia inducible factor HIF-1 promotes myeloid-derived suppressor cells accumulation through ENTPD2/CD39L1 in hepatocellular carcinoma. *Nat. Commun.* **8**, 517 (2017).
15. Dhanasekaran, R. et al. MYC Overexpression drives immune evasion in hepatocellular carcinoma that is reversible through restoration of proinflammatory macrophages. *Cancer Res.* **83**, 626–640 (2023).
16. Wheeler, D. A. & Roberts, L. R. Comprehensive and integrative genomic characterization of hepatocellular Carcinoma. *Cell* **169**, 1327–1341 (2017).
17. Chen, L. et al. Deep whole-genome analysis of 494 hepatocellular carcinomas. *Nature* **627**, 586–593 (2024).
18. Thompson, J. C. et al. Gene signature of antigen processing and presentation machinery predicts response to checkpoint blockade in non-small cell lung cancer (NSCLC) and melanoma. *J. Immunother. Cancer* **8**, https://doi.org/10.1136/jitc-2020-000974 (2020).
19. Ozga, A. J., Chow, M. T. & Luster, A. D. Chemokines and the immune response to cancer. *Immunity* **54**, 859–874 (2021).
20. Gao, Q. et al. Cancer-cell-secreted CXCL11 promoted CD8 + T cells infiltration through docetaxel-induced-release of HMGB1 in NSCLC. *J. Immunother. Cancer* **7**, 1–17 (2019).
21. López, M. D. et al. The relationship between chemokines CCL2, CCL3, and CCL4 with the tumor microenvironment and tumor-associated macrophage markers in colorectal cancer. *Tumor Biol.* **40**, 1–12 (2018).
22. Xue, R. et al. Liver tumour immune microenvironment subtypes and neutrophil heterogeneity. *Nature* **612**, 141–147 (2022).
23. Atkins, D. et al. MHC class I antigen processing pathway defects, ras mutations and disease stage in colorectal carcinoma. *Int. J. Cancer* **109**, 265–273 (2004).
24. El-Jawhari, J. J. et al. Blocking oncogenic RAS enhances tumour cell surface MHC class I expression but does not alter susceptibility to cytotoxic lymphocytes. *Mol. Immunol.* **58**, 160–168 (2013).
25. Franklin, D. A., James, J. L., Axelrod, M. L. & Balko, J. M. MEK inhibition activates STAT signaling to increase breast cancer immunogenicity via MHC-I expression. *Cancer Drug Resist.* **3**, 603–612 (2020).
26. Xiong, Z. et al. Targeting PPAR-gamma counteracts tumour adaptation to immune-checkpoint blockade in hepatocellular carcinoma. *Gut* **72**, 1758–1773 (2023).
27. Loboda, A. et al. A gene expression signature of RAS pathway dependence predicts response to PI3K and RAS pathway inhibitors and expands the population of RAS pathway activated tumors. *BMC Med. Genomics* **3**, https://doi.org/10.1186/1755-8794-3-26 (2010).
28. Zhu, A. X. et al. Molecular correlates of clinical response and resistance to atezolizumab in combination with bevacizumab in advanced hepatocellular carcinoma. *Nat. Med.* **28**, 1599–1611 (2022).
29. Ostrem, J. M. & Shokat, K. M. Direct small-molecule inhibitors of KRAS: From structural insights to mechanism-based design. *Nat. Rev. Drug Discov.* **15**, 771–785 (2016).
30. Zhu, C. et al. Targeting KRAS mutant cancers: from druggable therapy to drug resistance. *Mol. Cancer* **21**, 1–19 (2022).
31. Canon, J. et al. The clinical KRAS(G12C) inhibitor AMG 510 drives anti-tumour immunity. *Nature* **575**, 217–223 (2019).
32. Ketcham, J. M. et al. Design and discovery of MRTX0902, a potent, selective, brain-penetrant, and orally bioavailable inhibitor of the SOS1:KRAS protein-protein interaction. *J. Med. Chem.* **65**, 9678–9690 (2022).
33. Khare, S. et al. Abstract 3499: Inhibition of SOS1 by MRTX0902 augments the anti-tumor response of the targeted EGFR inhibitor osimertinib in NSCLC. *Cancer Res.* **87**, 3499 (2023).
34. Jeong, W. J., Ro, E. J. & Choi, K. Y. Interaction between Wnt/β-catenin and RAS-ERK pathways and an anti-cancer strategy via degradations of β-catenin and RAS by targeting the Wnt/β-catenin pathway. *NPJ Precis. Oncol.* **2**, 5 (2018).
35. Berasain, C. & Avila, M. A. The EGFR signalling system in the liver: From hepatoprotection to hepatocarcinogenesis. *J. Gastroenterol.* **49**, 9–23 (2014).
36. Dietrich, P. et al. Wild type Kirsten rat sarcoma is a novel microRNA-622-regulated therapeutic target for hepatocellular carcinoma and contributes to sorafenib resistance. *Gut* **67**, 1328–1341 (2018).

37. Xiong, H. J. et al. Elevated FBXL6 activates both wild-type KRAS and mutant KRASG12D and drives HCC tumorigenesis via the ERK/mTOR/PRELID2/ROS axis in mice. *Mil. Med. Res.* **10**, 1–21 (2023).
38. Xu, W. et al. Ribosome profiling analysis identified a KRAS-interacting microprotein that represses oncogenic signaling in hepatocellular carcinoma cells. *Sci. China Life Sci.* **63**, 529–542 (2020).
39. Jung, Y. H. et al. KCTD17-mediated Ras stabilization promotes hepato-cellular carcinoma progression. *Clin. Mol. Hepatol.* **30**, 895–913 (2024).
40. Rebouissou, S. & Nault, J. C. Advances in molecular classification and precision oncology in hepatocellular carcinoma. *J. Hepatol.* **72**, 215–229 (2020).
41. Kortlever, R. M. et al. Myc Cooperates with ras by programming inflammation and immune suppression. *Cell* **171**, 1301–1315 (2017).
42. Liao, W. et al. KRAS-IRF2 axis drives immune suppression and immune therapy resistance in colorectal cancer. *Cancer Cell* **35**, 559–572 (2019).
43. Kemp, S. B. et al. Efficacy of a small-molecule inhibitor of KrasG12D in immunocompetent models of pancreatic cancer. *Cancer Discov.* **13**, 298–311 (2023).
44. Mugarza, E. et al. Therapeutic KRASG12C inhibition drives effective interferon-mediated antitumor immunity in immunogenic lung cancers. *Sci. Adv.* **8**, https://doi.org/10.1126/sciadv.abm8780 (2022).
45. Mahadevan, K. K. et al. KRASG12D inhibition reprograms the microenvironment of early and advanced pancreatic cancer to promote FAS-mediated killing by CD8+ T cells. *Cancer Cell* **41**, 1606–1620 (2023).
46. Chen, N. et al. KRAS mutation-induced upregulation of PD-L1 mediates immune escape in human lung adenocarcinoma. *Cancer Immunol. Immunother.* **66**, 1175–1187 (2017).
47. Stopfer, L. E. et al. MEK inhibition enhances presentation of targetable MHC-I tumor antigens in mutant melanomas. *Proc. Natl. Acad. Sci. USA* **119**, e2208900119 (2022).
48. Chandrasekaran, S. et al. Phosphoinositide 3-kinase signaling can modulate MHC Class i and II expression. *Mol. Cancer Res.* **17**, 2395–2409 (2019).
49. Kitajima, S. et al. Suppression of STING associated with lkb1 loss in KRAS-driven lung cancer. *Cancer Discov.* **9**, 34–45 (2019).
50. Reschke, R. & Gajewski, T. F. CXCL9 and CXCL10 bring the heat to tumors. *Sci. Immunol.* **7**, 7–10 (2022).
51. Klampfer, L. et al. Oncogenic Ki-Ras inhibits the expression of interferon-responsive genes through inhibition of STAT1 and STAT2 expression. *J. Biol. Chem.* **278**, 46278–46287 (2003).
52. Li, N. et al. Cross-talk between TNF-α and IFN-γ signaling in induction of B7-H1 expression in hepatocellular carcinoma cells. *Cancer Immunol. Immunother.* **67**, 271–283 (2018).
53. Wu, X. Q. et al. Intestinal Akkermansia muciniphila complements the efficacy of PD1 therapy in MAFLD-related hepatocellular carcinoma. *Cell Rep. Med.* **6**, 101900 (2025).
54. Ju, H. L. et al. Transgenic mouse model expressing P53R172H, luciferase, EGFP, and KRASG12D in a single open reading frame for live imaging of tumor. *Sci. Rep.* **5**, 8053 (2015).
55. Li, B. & Colin N. Dewey. RSEM: accurate transcript quantification from RNA-Seq data with or without a reference genome. *BMC Bioinform.* **12**, https://doi.org/10.1186/1471-2105-12-323 (2011).
56. Ru, B. et al. TISIDB: An integrated repository portal for tumor-immune system interactions. *Bioinformatics* **35**, 4200–4202 (2019).
57. Leung, C. O. N. et al. Broad-spectrum kinome profiling identifies CDK6 upregulation as a driver of lenvatinib resistance in hepatocellular carcinoma. *Nat. Commun.* **14**, 6699 (2023).

Acknowledgements

This project is supported by RGC Theme-based Research Scheme (RGC TRS T12-705-24-R) and RGC Collaborative Research Fund (C5017-24G). We also acknowledge the University Research Facility in Life Sciences at Hong Kong Polytechnic University for providing and maintaining the equipment as well as the technical support needed for imaging work, and the Centralised Animal Facility at Hong Kong Polytechnic University for supporting our animal studies. We would like to thank the University Research Facility in Chemical and Environmental Analysis for providing technical support and maintaining the mass spectrometry equipment. We thank Dr. Amaia Lujambio (Icahn School of Medicine, Mount Sinai) and Dr. Weonsang Simon Ro (Kyung Hee University, Korea) for sharing the plasmids used for hydrodynamic tail vein injection. We also thank the Department of Pathology at the University of Hong Kong for the histopathology service.

Author contributions

M.M.L. and T.K.L. designed the experiment. M.M.L., C.O.L., R.W.L., X.Q.W., C.K.P., G.C.Y., W.K.C., J.L.N. and N.J.T. performed the experiment. M.M.L., S.M., M.T., G.S.L., S.L.C., Z.W.X., P.P.W., A.S.C., M.S.C., Q.H.M. and T.K.L. analysed the data, M.M.L. and T.K.L. wrote the paper. J.P.Y. and J.D. provided reagents and tissue samples for this study. T.K.L. supervised the study. All authors contributed to the discussion of results and manuscript corrections.

Competing interests

The authors declare no competing interests.

Additional information

Supplementary information The online version contains supplementary material available at https://doi.org/10.1038/s41467-025-64860-7.

Correspondence and requests for materials should be addressed to Terence Kin Wah Lee.

Peer review information *Nature Communications* thanks Naoto Fujiwara and the other anonymous reviewer(s) for their contribution to the peer review of this work. A peer review file is available.

[1]Department of Applied Biology and Chemical Technology, The Hong Kong Polytechnic University, Hong Kong, China. [2]School of Biomedical Sciences, Li Ka Shing Faculty of Medicine, The University of Hong Kong, Hong Kong, China. [3]School of Biomedical Sciences, The Chinese University of Hong Kong, Hong Kong, China. [4]Department of Pathology, Sun Yat-Sen University Cancer Center, Guangzhou, China. [5]Department of Medicine, Li Ka Shing Faculty of Medicine, The University of Hong Kong, Hong Kong, China. [6]Department of Clinical Oncology, Sir YK Pao Centre for Cancer, The Chinese University of Hong Kong, Hong Kong, China. [7]Clinical Cancer Institute, Center for Translational Medicine, Naval Medical University, Shanghai, China. [8]State Key Laboratory of Liver Research, The University of Hong Kong, Hong Kong, China. [9]Research Institute for Future Food, The Hong Kong Polytechnic University, Hong Kong, China.
✉e-mail: terence.kw.lee@polyu.edu.hk